

2017-01-01

# Bragg Gratings In Polarization Maintaining Optical Fiber As Three Dimensional Strain Sensor

Joel Quintana

University of Texas at El Paso, joel.jquintana@gmail.com

Follow this and additional works at: [https://digitalcommons.utep.edu/open\\_etd](https://digitalcommons.utep.edu/open_etd)



Part of the [Electrical and Electronics Commons](#), and the [Optics Commons](#)

---

## Recommended Citation

Quintana, Joel, "Bragg Gratings In Polarization Maintaining Optical Fiber As Three Dimensional Strain Sensor" (2017). *Open Access Theses & Dissertations*. 337.

[https://digitalcommons.utep.edu/open\\_etd/337](https://digitalcommons.utep.edu/open_etd/337)

This is brought to you for free and open access by DigitalCommons@UTEP. It has been accepted for inclusion in Open Access Theses & Dissertations by an authorized administrator of DigitalCommons@UTEP. For more information, please contact [lweber@utep.edu](mailto:lweber@utep.edu).

BRAGG GRATINGS IN POLARIZATION MAINTAINING OPTICAL FIBER  
AS THREE DIMENSIONAL STRAIN SENSOR

JOEL QUINTANA

Doctoral Program in Electrical and Computer Engineering

APPROVED:

---

Virgilio Gonzalez, Ph.D., Chair

---

Jack Chessa, Ph.D.

---

Raymond Rumpf, Ph.D.

---

Benjamin C. Flores, Ph.D.

---

Charles Ambler, Ph.D.  
Dean of the Graduate School

©Copyright

by

Joel Quintana

2017

*to my*

*DAUGHTER, WIFE, MOTHER, FATHER, and BROTHER*

*with love*



BRAGG GRATINGS IN POLARIZATION MAINTAINING OPTICAL FIBER  
AS THREE DIMENSIONAL STRAIN SENSOR

by

JOEL QUINTANA

DISSERTATION

Presented to the Faculty of the Graduate School of

The University of Texas at El Paso

in Partial Fulfillment

of the Requirements

for the Degree of

DOCTOR OF PHILOSOPHY

Doctoral Program in Electrical and Computer Engineering

THE UNIVERSITY OF TEXAS AT EL PASO

MAY 2017

# Acknowledgements

I would like to thank my family for their support and love. My loving mother, Rosalia and all her sacrifice. My father, Rafael (r.i.p) who always said *I'm proud of you, son*. My brother, René who I look up to. Always.

I would like to thank my wife Marcy, you are everything to me. All my accomplishments, all my defeats are met by you with love and support. I am absolutely elated to start this new stage in our lives with our baby Inés, Marty and Maggie.

I would like to thank my committee Dr. Virgilio Gonzalez, Dr. Jack Chessa, Dr. Raymond Rumpf and Dr. Benjamin Flores.

Virgilio - Thank you for your unrelenting support, motivating and trust. Every opportunity I've had to move forward in my career have been thanks to you. Your advice is invaluable and I hold it dear to my heart.

Jack - Thank you for your absolute selflessness. Your insight, expertise and support was invaluable to this research. You did all of this, expecting nothing in return. And for that, I'm forever in your debt. Looking forward to sitting in on some jazz sessions soon.

Tipper - Your courses allowed me to understand my research topic to its fullest extent. I leave this university with a greater knowledge base because of you. Your work in the fields of research and academia are truly an inspiration.

Ben - It's All But Dissertation from here on out. Thank you for all your advice throughout my time at UTEP.

This research was funded by the NASA Science and Technology Institute for Minority Institutions (NSTI), award number NNX09AV17A. I'd like to acknowledge the support of Dr. Curtis Banks at Marshall Space Flight Center, Dr. Calvin M. Stewart, Dr. Miguel Velez-Reyes, and Dr. Ivonne Santiago.

# Abstract

Fiber-Bragg Gratings (FBG) for Structural Health Monitoring (SHM) have been studied extensively as they offer electrically passive operation, electromagnetic interference (EMI) immunity, high sensitivity and multiplexing as compared to conventional electric strain sensors. FBG sensors written within polarization maintaining (PM) optical fiber offer additional dimensions of strain measurement, greatly reducing the number of sensors needed to properly monitor a structure. This reduction however, adds complexity to the discrimination of the sensor's optical response to its corresponding applied strains. This dissertation defines the set of algorithms needed to measure planar strain using PM-FBGs exclusively. It defines the minimum number of sensors needed to reconstruct the full state of strain,  $\bar{\epsilon}$  and the maximum number of strain tensor components a single PM-FBG is capable of measuring. Two experiments were performed under the same test specifications; a single PM-FBG and 2 multiplexed PM-FBGs in a rosette pattern adhered to a test specimen subject to uniaxial tension. The far field strain was measured at the location of the sensor using only the optical response and PM-FBG axes orientation with respect to the specimen axes. Strains at the surface of the specimen were measured using Digital Image Correlation (DIC) analysis and an electronic extensometer. The PM-FBG measurements were then compared to the DIC/extensometer data for validation. The comparison of the strains  $\epsilon_{xx}$ ,  $\epsilon_{yy}$ , and  $\epsilon_{xy}$  resulted in a high correlation, averaging .97 between the strain measurement techniques. The PM-FBG measured specimen surface strains with low percent error values (approximately 20%). PM-FBG sensitivity is greatly affected by the sensor's material properties and installation or embedding techniques. The algorithm for measuring a full state of planar strain at a point presented in this dissertation and is validated through experimental analysis. It can be applied to multiple or single PM-FBG systems with low error and high correlation to actual strains on the surface of a specimen. It is the first step in practical implementation of PM-FBGs for Structural Health Monitoring.

# Table of Contents

	Page
Acknowledgements . . . . .	v
Abstract . . . . .	vi
Table of Contents . . . . .	vii
List of Tables . . . . .	ix
List of Figures . . . . .	x
<b>Chapter</b>	
1 Introduction . . . . .	1
1.1 Research Question . . . . .	3
2 Background and Literature Review . . . . .	4
2.1 Literature Review . . . . .	4
2.1.1 Optical Fiber . . . . .	4
2.1.2 Fiber Bragg Gratings . . . . .	5
2.1.3 Polarization Maintaining FBG strain sensors. . . . .	5
2.1.4 Fiber Bragg Grating Strain Sensor . . . . .	8
2.2 Electromagnetic Theory of Fiber Bragg Gratings . . . . .	12
2.2.1 Maxwell's Equations . . . . .	12
2.2.2 Wave Equation . . . . .	13
2.2.3 Polarization . . . . .	15
2.2.4 Guided Waves . . . . .	17
2.2.5 Single-mode Optical Fiber . . . . .	18
2.2.6 Single-mode Polarization Maintaining Optical Fiber . . . . .	19
2.2.7 Fiber Bragg Gratings . . . . .	20
2.3 Strain Analysis . . . . .	23
2.3.1 Strain Gauge . . . . .	26

2.3.2	Strain Transformation . . . . .	27
3	Mounted PM-FBG Sensor . . . . .	30
3.1	Single PM-FBG . . . . .	30
3.1.1	Optical Interrogation . . . . .	33
3.1.2	Strain Transformations . . . . .	34
3.1.3	Strain Lag and Transfer Rate . . . . .	37
3.2	PM-FBG Rosette . . . . .	39
3.2.1	Optical Interrogation . . . . .	40
3.2.2	Strain Transformations . . . . .	41
3.2.3	Strain Lag and Transfer Rate . . . . .	41
4	Experiment Results and Analysis . . . . .	45
4.1	Single PM-FBG . . . . .	45
4.2	PM-FBG Rosette . . . . .	50
5	Concluding Remarks . . . . .	57
5.1	Future Work . . . . .	59
	References . . . . .	60
	<b>Appendix</b>	
A	Glossary . . . . .	65
	Curriculum Vitae . . . . .	66

# List of Tables

3.1	Single PM-FBG Material Properties . . . . .	31
3.2	PM-FBG Rosette Material Properties . . . . .	43
4.1	Single PM-FBG Sensor Measurement Error, Std. Deviation, % Error . . .	48
4.2	Single PM-FBG Sensor Measurement Percent (%) Error Across Load . . .	49
4.3	FBG Rosette Sensor Locations . . . . .	52
4.4	Rosette PM-FBG Sensor Measurements Error, Std. Deviation, % Error . .	56
4.5	Rosette PM-FBG Sensor Measurement Percent (%) Error Across Load . .	56

# List of Figures

2.1	Fiber Bragg grating in single-mode fiber subject to elongation along the longitudinal axis of the fiber. . . . .	9
2.2	Fiber Bragg Grating in PM optical fiber, 3-axis nomenclature. . . . .	10
2.3	PM FBG - baseline and strained reflected spectra . . . . .	11
2.4	Polarization . . . . .	16
2.5	Dielectric slab waveguide . . . . .	17
2.6	Snell's Law and Total Internal Reflection . . . . .	18
2.7	Single-mode optical fiber . . . . .	19
2.8	Polarization maintaining single-mode optical fiber . . . . .	20
2.9	Fiber Bragg grating in single-mode optical fiber, $n_c$ is the effective refractive index of the core, and $n_f$ is that of the Bragg grating variation. . . . .	21
2.10	Fiber Bragg Grating Optical Response . . . . .	21
2.11	One-dimensional strain . . . . .	23
2.12	Undeformed and deformed cube of material in 3D. Shear strains are zero so angles are preserved. Displacement vector $\mathbf{P} \rightarrow \mathbf{P}'$ has components $u, v, w$ and $x, y, z$ , respectively. . . . .	24
2.13	Two-dimensional deformation and strain showing shear strain. . . . .	25
2.14	Foil resistive strain gauge . . . . .	27
2.15	Strain gauge rosette . . . . .	28
2.16	Rosette angles . . . . .	28
2.17	Strain axis transformation . . . . .	29
3.1	Strain evaluation algorithm . . . . .	31

3.2	ASTM-D638 polycarbonate specimen with (a) PM-FBG adhered with epoxy, (b) DIC speckle pattern, (c) 50N $\varepsilon_{yy}$ strain field with location of PM-FBG orientation of the fiber $\varepsilon_a - 10^\circ$ from primary axis strain $\varepsilon_{yy}$ . . . . .	32
3.3	Optical test bench . . . . .	34
3.4	External strains $\varepsilon_{y'}$ and $\varepsilon_{z'}$ on the cross section of a PM optical fiber with $\phi^\circ$ between the slow axis and the surface plane . . . . .	35
3.5	PM-FBG sensor with its axial $\epsilon_a$ and parallel to surface slow $\epsilon_s$ axes, placed on $\theta^\circ$ and $\theta^\circ + 90^\circ$ from the external principle strains $\epsilon_{xx}$ and $\epsilon_{yy}$ respectively	36
3.6	Diagram of symmetrical sections for the fiber adhered by epoxy resin, axial and cross sectional views. . . . .	38
3.7	Three-FBG sensor in PM optical fiber . . . . .	39
3.8	ASTM-D638 polycarbonate specimen with (a) PM-FBG adhered with epoxy, (b) DIC speckle pattern, . . . . .	40
3.9	Modified optical interrogation system . . . . .	42
3.10	PM-FBG rosette location on strain field and gauge angles compared to XY axis . . . . .	43
3.11	Cross section of FBG 2 and 3 showing distance of sensor to specimen surface.	44
4.1	DIC measurements $\varepsilon_x$ left, $\varepsilon_y$ center, $\varepsilon_{xy}$ right. . . . .	46
4.2	DIC Strain, $\varepsilon_x$ (blue), $\varepsilon_{xy}$ (red), $\varepsilon_y$ (green), extensometer . . . . .	47
4.3	Mounted PM-FBG optical wavelength shift response at 5 - 2000 N specimen loads with fast green and slow blue axes. . . . .	48
4.4	Sensor cross-section, $\varphi = -17^\circ$ . . . . .	49
4.5	Sensor(dashed line) and DIC strain(solid line) or Extensometer in y direction vs. load . . . . .	50
4.6	Single PM-FBG Error across load DIC/Extensometer (dashed) to FBG(red)	51
4.7	Cross section of FBG 2 and 3 showing distance of sensor to specimen surface.	52



4.8	Mounted PM-FBG rosette optical wavelength shift response at 0 - 2000 N specimen loads with fast green and slow blue axes. FBG2 is on the right, FBG3 is on the left. . . . .	53
4.9	$\varepsilon_{xx}$ sensor measurements per strain axis vs. load . . . . .	54
4.10	$\varepsilon_{yy}$ sensor measurements per strain axis vs. load . . . . .	54
4.11	$\varepsilon_{xy}$ sensor measurement per strain axis vs. load . . . . .	55
4.12	Out-of-plane sensor measurements per strain axis vs. load . . . . .	56
5.1	Strain evaluation algorithm . . . . .	57

# Chapter 1

## Introduction

Structural Health Monitoring (SHM) had its inceptions in the early 19th century, when railroad Wheel-tappers would evaluate damage on steel rails by characterizing the sound of a hammer striking against a railcar wheel. In more than a century, this practice has evolved to include mechanical, acoustic, electrical and even photonic sensors both simple and complex in their compositions and use. We also find ourselves using ever-changing materials and complex structures exposed to more-and-more strenuous environments. One such material, the S-Glass/epoxy unidirectional composite, for example, offers approximately fifty percent more tensile strength than AISI-1045 steel yet is a quarter of the density. When compared to 6101-T6 Aluminum, the same composite offers approximately four times the tensile strength for approximately two-thirds of the weight[1]. Composite materials however, are not without their disadvantages. Most notably, their anisotropic behavior to applied stresses lead to unpredictable-catastrophic failure once a failure mode is initiated. Engineering design requirements and safety regulations throughout the years have become more rigorous and invite the need to evaluate structures more precisely, especially if human interaction with the structure is present and constant. With the recent prevalence of hybrid composite laminated or fully composite, reusable rocket structures, it is of critical need to evaluate the structural health of each rocket before, after and possibility during each launch. Given composites failure habits, the rate of dissemination of composite materials in our daily lives, and the importance of human safety, research in precise SHM of composite structures is key in the wide spread implementation of composite materials. The geometry of the fibers that make up composite structures and their intrinsic dielectric properties make fiber optic sensors (FOSs) the ideal sensing tool for SHM. Fiber

optic sensors are conventional optical fibers primarily used for communications, which exhibit a secondary function as a sensing element. Examples of FOSs are the Fabry-Pérot interferometer and the fiber Bragg grating (FBG). A FBG sensor can be adhered at the surface of the structure, embedded between layers of preforms or inter-woven between individual strands effectively becoming a part of the structure. In the last three decades, a great number of studies have been published on FBGs written in single-mode (SM) and in single-mode polarization-maintaining (PM) optical fibers for strain measurements. These studies resulted in well-documented models for the FOS relating external strains applied on the core and their optical waveguide properties. Investigations on embedding of SM and PM FBG sensors in composite materials have also been published. The proceeding section in this chapter delineates these studies. And while SM FBG sensors have experienced an increase in popularity in its use in sensing topologies, PM FBG sensors, despite the PM FBG's ability to sense external strains in all spatial directions vs. SM's uniaxial strain response, has yet to follow suit. Strain fields due to applied stress rarely are in one direction. So if PM FBG sensors are better suited to simultaneously detect strains in multiple directions, why not the widespread adoption of the multi-axial sensor? It turns out that the practical implementation of the PM FBG sensor is not without its challenges. For example, due to how PM optical fiber is manufactured to achieve its namesake property, the FBG sensor written in the optical fiber is rotation sensitive. The strain measurement at any given point is dependent on the axial rotation of the fiber with respect to the structure it's adhered to. Knowledge of the sensor rotational orientation must be known in order to correlate the optical response to the measured mechanical strain. Precise installation of the PM FBG sensor on the host structure is paramount, making sensor installation an extremely difficult and costly process. Despite this seemingly insurmountable hurdle, PM FBG offer considerable advantages over SM FBG sensors such as multi-parameter sensing [29], sensor number minimized sensor quantities [3], and fault location [4].

## 1.1 Research Question

This dissertation attempts to answer the following question: Using Fiber Bragg Gratings written to the core of Polarization Maintaining, Single Mode optical fiber, can the full state of strain of a structure at the sensor location be reconstructed by exclusively interrogating the optical response of the strain sensor? What are the minimum requirements to do so? The examination of this objective includes theoretical models derived from literature review and experimental investigations.

# Chapter 2

## Background and Literature Review

This chapter reviews selected past works on FBGs in single-mode and polarization maintaining as strain sensors. The objective of this section is to provide historical and current state-of-the-art context. An analytical foundation to the work presented in this document. The contents in the sections following the literature review in 2.1 were compiled with the intent of giving the reader the appropriate background to the electrodynamics governing the optical sensor presented in this dissertation. The relationship between the mechanical strains on the FBG sensor and its optical response involves all that is covered here. I encourage the reader to refer to the cited references for detailed derivations and proofs.

### 2.1 Literature Review

#### 2.1.1 Optical Fiber

In 1981, in the publication *Stress Analysis Of Optical Fibers By A Finite Element Method*, Katsunari Okamoto, et. al. [23] investigated stress-induced birefringence in single-mode optical fibers having arbitrary core shape. Using the Finite Element Method, they calculated modal birefringence due stress caused by external forces in noncircular core fibers. In the work, *Determination of the Individual Strain-Optic Coefficients in Single-Mode Optical Fibers* by Axel Bertholds and Rene Dandliker [24], the pair determine the individual strain-optic coefficients in single-mode optical fibers. For an optical fiber with a pure silica core and a cladding doped with BZ03 (LT-FI506B), the strain-optic coefficients have been measured to be  $P_{l1} = 0.133$ , and  $P_{l2} = 0.252$ , respectively. These measurements have been

proven to be quite accurate, are quite essential to the calculation of strains and see wide spread use today.

### **2.1.2 Fiber Bragg Gratings**

We now turn our attention to the fiber Bragg gratings, written in single-mode optical fiber. *Fiber Bragg Grating Technology Fundamentals and Overview* [25] contains an introduction to the fundamentals of FBG's, including a description of techniques for grating fabrication and a discussion of those fiber photosensitivity characteristics, which underlie grating formation. Kenneth O. Hill and Gerald Meltz highlight the salient properties of periodic, optical waveguide structures that are used in the design of grating filters and conclude with an overview of key applications in optical telecommunications and quasi-distributed, thermo-physical measurement. Alan D. Kersey et. al. [18], provided a comprehensive overview of FBG sensors in *Fiber Grating Sensors*. The group reviews developments in the area of grating based sensors, including basic quasi-distributed sensors based on Bragg gratings, chirped grating sensing, fiber Bragg grating laser sensors, long-period grating sensors and interferometric configurations based on gratings. The techniques discussed will primarily be focused on the measurement of strain, but systems have also been used for temperature measurements. Although this dissertation does not account for the effects of temperature on strain measurements, it is prudent to mention the studies found on FBG sensor temperature dependence. Robert R J Maier et. al [26], does just that.

### **2.1.3 Polarization Maintaining FBG strain sensors.**

The dissertation by C. Lawrence [27] presents the use of a FBG sensor in single mode optical fiber in measuring residual stresses generated by the curing process of composite structures. This is done by analyzing the strains induced in the optical fiber core within the region of the FBG. This study leads to discovery of the limitations of a FBG strain sensor, most notably, the ability of the sensor to accurately measure one parameter at any time. Lawrence goes

on to suggest the use of two overwritten FBGs with different Bragg wavelengths written in PM fiber core instead. Theoretically, this multi-parameter optical sensor can measure the three primary strains and temperature via behavior of the 4 optical peaks present. Lawrence assumes a linear behavior between the mechanical strains on the fiber core at the FBG region and the Bragg wavelength. Mohanraj Prabhugoud, et. al in *Finite element model for embedded fiber Bragg grating sensor* [28] present an integrated formulation for the calculation of the spectral response of a fiber Bragg grating sensor as a function of the strain. In particular, they calculate the transverse strain sensitivity of a fiber Bragg grating sensor through the calculation of the change in effective index (or indices) of refraction of the fiber cross-section. Tadamichi Mawatari [29] presented mathematical models for predicting strain in a multi-parameter optical sensor. The linear and non-linear models were built from wavelength data collected on 3 different specimens subject to temperature, axial, transversal, and simultaneous axial/transversal loading. This work showed the shift in the Bragg wavelengths, exhibits a linear relationship when compared to the change in load exerted on the fiber in that direction. This linearity is present for temperature, axial, and transversal loading dimensions. The experimental data show slight non-linearity when simultaneous axial and transversal loads are present on the fiber, the linear model however can still accurately predict Bragg wavelength shifts due to simultaneous loads in the axial and transversal directions. According the work presented in this body of work; axial rotation of the fiber sensor fast and slow axes is the biggest contributor to the non-linear behavior. In the publication *Characterization of the response of fiber Bragg grating sensors subjected to a two-dimensional strain field* [30], the behavior of fiber Bragg grating sensors subjected to transversal as well as axial strains was again characterized for polarization-maintaining single-mode optical fibers. Diametrical compression is studied, embedded in an epoxy specimen and their response monitored when subjected to biaxial loading. The experimental results are compared to those obtained by means of finite-element simulations and an appropriate analytical description of the opto-mechanical response of polarization-maintaining fibers is described. The work describes a number of intrinsic drawbacks and

practical difficulties when using PM FBG sensors such as the nonlinear behavior when diametrical compression is applied at an angle to the principal axes. The fast and slow axes in PM fibers display a difference in sensitivity when subjected to diametrical compression. The transversal sensitivity of the sensors is considerably smaller than the longitudinal one. And, the embedded PM-fiber sensors display a marked sensitivity with respect to the embedding angle. With the publication *Shear Strain Influence on Fiber Bragg Grating Measurement Systems* [31] Mathias Stefan Müller and company proved that shear strains do influence the spectral response of fiber Bragg sensors and compute the direct influence on the spectral output. Studying the effects of unpolarized light to the FBG shear strain problem they show that for unpolarized light, shear strains have to be taken into account as well. They applied full tensor coupled-mode theory to compute the optical response of a mechanically loaded FBG in a polarization-maintaining fiber in the presence of strong shear strains. For several load scenarios, they calculated the output spectrum for the two polarization modes. They found a reduced influence of shear strain in fibers with high birefringence (i.e. PM optical fiber). They conclude that shear strains have to be considered as a parameter influencing the output of an FBG measurement system. Depolarizing the light source does not cancel the shear strain effects and since five parameters are actually influencing the spectral response significantly, the four parameters derived from [35] will not suffice to reconstruct the state of strain. It may be observed that the relative power of the polarization reflection peaks depends on the applied shear strain. It may therefore be possible to directly measure the shear strain component from the relative intensities of the two Bragg peaks. A Pérez Grassi et. al. state in [22] that research efforts in Fiber Bragg grating (FBG) sensors have been directed towards reconstruction of the strain tensor of a host material at the position of the FBG, using FBGs in polarization-maintaining fibers. His team employed a theoretical description of FBGs which also describe the influence of shear strain. They proposed an algorithm which allows for reconstructing the principal strains, as well as the shear strain components. Demonstrated by simulations, they find that under the presence of shear strains, one can use the induced polarization



mode coupling as a measure for the level of shear strain. They demonstrated how the strains are mathematically connected to the respective features in the reflection signals, namely the Bragg wavelengths  $\lambda_{B,s}$  and  $\lambda_{B,f}$  and defined polarization mode coupling coefficient  $Q_{11}$  and  $Q_{12}$ . A rugged reconstruction of the strains can be accomplished however, to the nature of the measurement process the reconstruction fails whenever the two Bragg peaks are spectrally close or overlapping. This is because no clear distinction between the polarization modes is possible. Another limitation of the reconstruction is obtaining the absolute value of the shear strain, which is due to the occurrence of the square of the shear strain in the derived equations.

### 2.1.4 Fiber Bragg Grating Strain Sensor

An FBG written to a single-mode optical fiber core reflects a single Bragg reflection peak of  $\lambda_B$  when a broadband light source is coupled in the core. As a one-directional strain sensor, the relationship between the engineering strain on the longitudinal (axial) axis,  $\varepsilon_a$  and the Bragg reflection is given by [18].

$$\varepsilon_a = \frac{\Delta\lambda_B}{\lambda_B \left[ 1 - \frac{n_0^2}{2}(p_{12} - \nu(p_{12} + p_{11})) \right]}. \quad (2.1)$$

The strain on the FBG region can be calculated from the ratio of the measured wavelength shift  $\Delta\lambda_B$  and the unstrained or baseline reflection wavelength  $\lambda_B$  along with the material properties for silica optical fiber. This includes the effective index of refraction  $n_0$ , which is the measure of the delay which light propagating through the medium experiences, compared to the propagation of light in vacuum. The *effective index of refraction* is a measure of the overall delay of a light propagating through the core/cladding of the optical fiber. This is not a property of the core or the cladding the optical fiber is made of, but an effective property of the fiber altogether. poisson's ratio  $\nu$ , is the signed ratio of transverse strain to axial strain. In other words, the amount of transversal expansion divided by the amount of axial compression. The photoelastic constants  $p_{12}$ ,  $p_{11}$  [24].

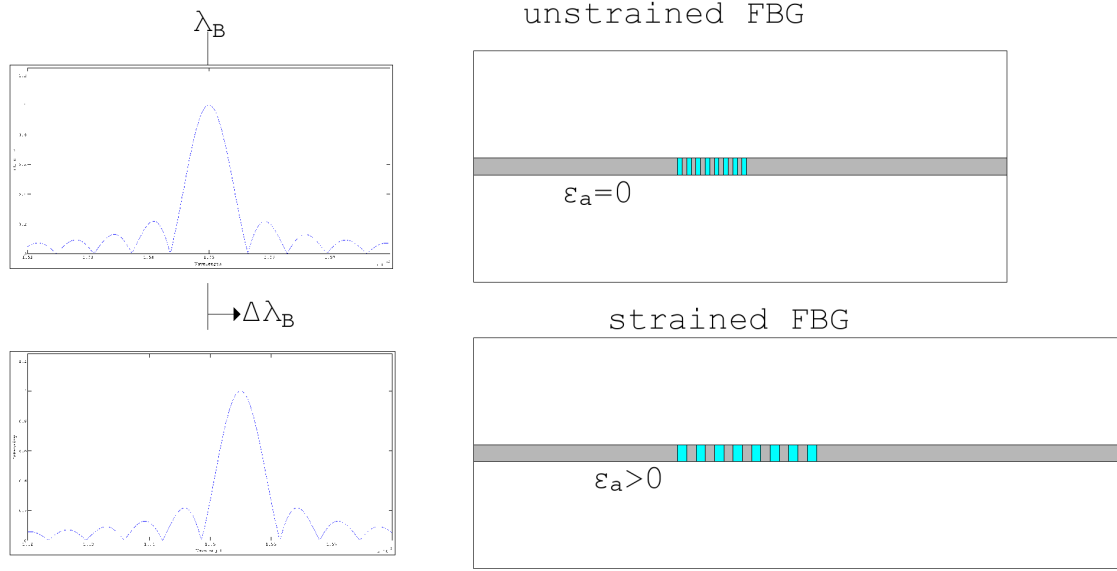


Figure 2.1: Fiber Bragg grating in single-mode fiber subject to elongation along the longitudinal axis of the fiber.

When that same FBG is written to a PM fiber core and broadband light is coupled into both orthogonal polarization axes of the core, two reflection peaks mirrored on  $\lambda_B$  occur,  $\lambda_{B,f}$  and  $\lambda_{B,s}$  [3]. This split in  $\lambda_B$  is due to the birefringence induced on the SM core by the PM fiber stress applying parts (SAP) during the fiber drawing process.

Due to the wavelength split, the measured wavelength shift  $\Delta\lambda_B$  and the baseline wavelength  $\lambda_B$  is now the mean of the slow and fast axis peaks from the baseline to the delta:

$$\lambda_B = \left| \frac{\lambda_{B,s} - \lambda_{B,f}}{2} \right| \quad (2.2)$$

and

$$\Delta\lambda_B = \left| \frac{\Delta\lambda_{B,s} - \Delta\lambda_{B,f}}{2} \right| \quad (2.3)$$

The Bragg response for axial strain is independent of any strains acting on the cross section of the fiber since the FBG properties are the same with respect to both polarization axes in

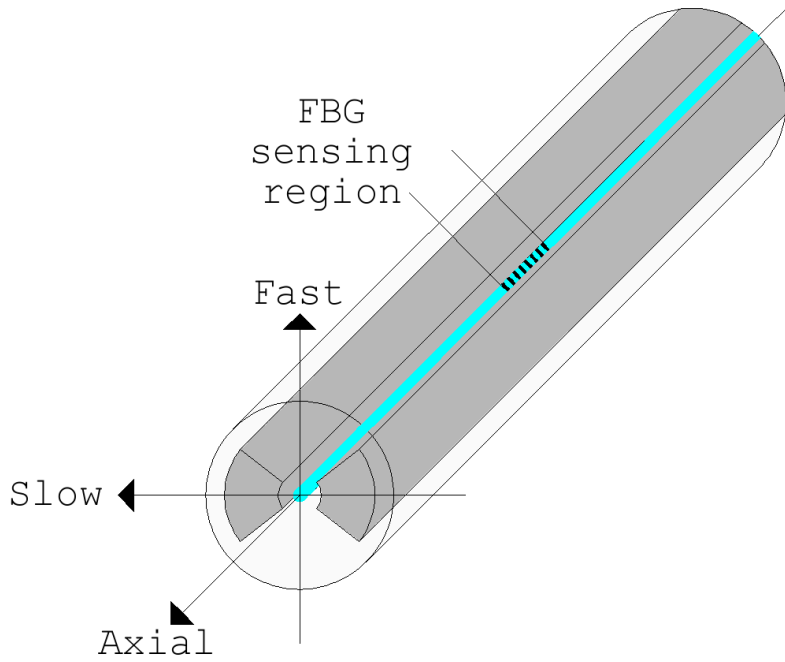


Figure 2.2: Fiber Bragg Grating in PM optical fiber, 3-axis nomenclature.

the fiber core [29]. The relationship between the Bragg reflections and the three orthogonal strains  $\epsilon_a$ ,  $\epsilon_s$ , and  $\epsilon_f$  in reference to the axial, slow and fast axes, respectively, in the region of the FBG in the optical fiber are characterized by the set of equations

$$\begin{aligned}\Delta\lambda_{B,s} &= \left[ \epsilon_a - \frac{n_s^2}{2}(p_{11}\epsilon_s + p_{12}\epsilon_f + p_{12}\epsilon_a) \right] \lambda_{B,s} \\ \Delta\lambda_{B,f} &= \left[ \epsilon_a - \frac{n_f^2}{2}(p_{11}\epsilon_f + p_{12}\epsilon_s + p_{12}\epsilon_a) \right] \lambda_{B,f}\end{aligned}\tag{2.4}$$

Using equations 2.7 and 2.8 to solve for  $\epsilon_a$  one can then solve the system of equations in 2.9 for  $\epsilon_s$ , and  $\epsilon_f$ . The interrelation between the unstrained Bragg peaks  $\lambda_{B,s,f}$  and the measured wavelength shifts for each peak  $\Delta\lambda_{B,s,f}$  are described in [20].

The shear strain  $\epsilon_{sf}$  on the cross section of the PM fiber has a different effect on the Bragg reflection when compared to  $\epsilon_a$ ,  $\epsilon_s$  or  $\epsilon_f$ . Fundamentally changing the fiber core permittivity  $\epsilon$ , the reflected optical signal undergoes a polarization mode coupling [31]. The power from one polarization axis couples onto the other, regardless of the light's

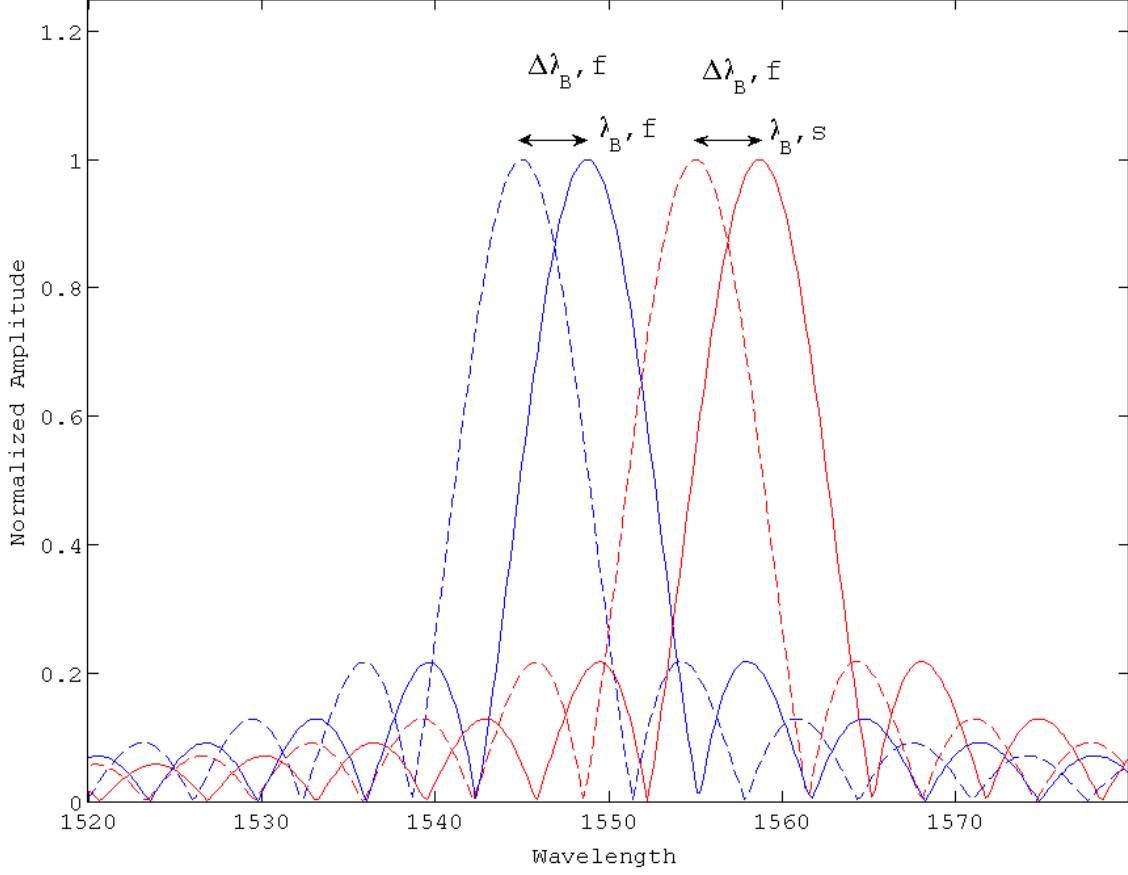


Figure 2.3: PM FBG - baseline and strained reflected spectra

polarization state inside the core. Determining  $\varepsilon_{sf}$  from the reflected Bragg signal requires calculating  $\epsilon$  from the reflected spectra in both polarization axes.

$$\varepsilon_{sf} = \frac{-2\epsilon}{(p_{11} - p_{12})n_s^2 n_f^2} \quad (2.5)$$

$$\epsilon = \frac{n_f^2(\lambda_{Bs}^2 - \lambda_{Bf}^2)}{\lambda_{Bf}^2(1 + \varepsilon_a)^2} \frac{\sqrt{\frac{Q_{11}}{Q_{12}}}}{\frac{Q_{11}}{Q_{12}} + 1} \quad (2.6)$$

The constants  $Q_{11}$  and  $Q_{12}$  are material constants determined by [22].

## 2.2 Electromagnetic Theory of Fiber Bragg Gratings

### 2.2.1 Maxwell's Equations

In 1873, Scottish physicist James Clark Maxwell developed the he fundamental equations of electrodynamics that govern all electric, magnetic, optic, and electromagnetic phenomena. Now known as Maxwell's equations [5]. These four equations completely govern the electromagnetic field and the medium that surrounds it.

$$\begin{aligned}\nabla \times \vec{E} + \frac{\partial \vec{B}}{\partial t} &= 0 \\ \nabla \times \vec{H} - \frac{\partial \vec{D}}{\partial t} &= \vec{J} \\ \nabla \cdot \vec{D} &= \rho \\ \nabla \cdot \vec{B} &= 0\end{aligned}\tag{2.7}$$

In these equations,  $\vec{E}$  and  $\vec{H}$  are the electric field vector and magnetic field vector, respectively. These vectors describe an electromagnetic field or an optical wave.  $\vec{D}$  and  $\vec{B}$  describe the effect of  $\vec{E}$  and  $\vec{H}$  on matter, known as the electric displacement and magnetic induction vectors.  $\rho$  and  $\vec{J}$  are the electric charge density and electric current density, respectively and may be considered the source of the electromagnetic radiation  $\vec{E}$  and  $\vec{H}$ . Within the realm of fiber optics, we deal with propagation and transmission of electromagnetic radiation that does not have an effect on the material it is contained in. If we set  $\rho = 0$  and  $\vec{J} = 0$  in equation 2.7, we find that non-zero solutions to Maxwell's equations exists, and electromagnetic radiation can exist in a space without the presence of electric charges or currents. Field vectors unique to a medium in which they are propagating, must be supplemented by the material equations or *constitutive relations* [6].

$$\begin{aligned}\vec{D} &= [\varepsilon]\vec{E} \\ \vec{B} &= [\mu]\vec{E}\end{aligned}\tag{2.8}$$

The  $\varepsilon$  and  $\mu$  parameters are  $3 \times 3$  matrices known as the permittivity and permeability tensors, respectively. If the material medium is isotropic, like in the case of optical fiber, both  $\varepsilon$  and  $\mu$  reduce to scalars. Permittivity is a measure of how an electric field affects, and is affected by, a dielectric medium. Permittivity is directly related is a measure of how easily a dielectric polarizes in response to an electric field and thus, relates to a material's ability to resist an electric field. Analogous to permittivity, permeability relates the same dielectric material to its magnetization when introduced to magnetic fields. The constant  $\varepsilon_0$  is called the free space or vacuum permittivity and is given by  $\varepsilon_0 = 8.854 \times 10^{-12} F/m$ . The free space permeability is  $\mu_0 = 4\pi \times 10^{-7} H/m$ .

### 2.2.2 Wave Equation

In fiber optic communications, one often deals with an electromagnetic carrier wave with a single angular frequency of oscillation, known as monochromatic light. The field vectors of monochromatic light are sinusoidal functions of time. Two of the most important results of Maxwell's equations are the wave equations and the existence of electromagnetic waves that are solution to them. Restricting the wave to a medium that is homogeneous and isotropic with both charge  $\rho$  and current  $\vec{J}$  density equal zero and using the constitutive relations  $\vec{D} = \varepsilon \vec{E}$  and  $\vec{B} = \mu \vec{H}$  the first two of Maxwell's equations are

$$\begin{aligned}\nabla \times \vec{E} + \mu\varepsilon \frac{\partial \vec{H}}{\partial t} &= 0 \\ \nabla \times \vec{H} - \varepsilon \frac{\partial \vec{E}}{\partial t} &= 0.\end{aligned}\tag{2.9}$$

We then get the wave equation for the electric field vector  $\vec{E}$  in a homogenous and isotropic media

$$\nabla^2 \vec{E} - \mu\varepsilon \frac{\partial^2 \vec{E}}{\partial t^2} = 0.\tag{2.10}$$

Likewise, the wave equation for the magnetic field vector in the media is

$$\nabla^2 \vec{H} - \mu\varepsilon \frac{\partial^2}{\partial t^2} \vec{H} = 0. \quad (2.11)$$

These are the standard electromagnetic wave equations satisfied by the monochromatic plane wave solution [5]

$$\Psi = Ae^{i(\omega t - \vec{r}\vec{k})} \quad (2.12)$$

where A is the amplitude and a constant. The angular frequency  $\omega$  is related to the wave vector  $\vec{k} = \omega\sqrt{\mu\varepsilon}$  and  $\Psi$  can be any Cartesian component of  $\vec{E}$  and  $\vec{H}$  such that

$$\begin{aligned} \vec{E} &= E_x \hat{a}_x + E_y \hat{a}_y + E_z \hat{a}_z \\ \vec{H} &= H_x \hat{a}_x + H_y \hat{a}_y + H_z \hat{a}_z. \end{aligned} \quad (2.13)$$

At any point in space, the given field is a sinusoid and a function of time. At any point in time, said field is a sinusoidal function of space. The fields have the same values for coordinates  $\vec{r}$  and time  $t$ . The fact that  $\omega t - \vec{r}\vec{k}$  is a constant, determines a plane normal to the wave vector  $\vec{k}$  at any instant of time. Equation 2.12 is called a plane wave. These planes are referred to as *wavefronts* and travel in the direction of  $\vec{k}$  with a phase velocity  $v = \omega/|\vec{k}|$ . The value of the phase velocity is a property of the medium and can be expressed in terms of the dielectric constant  $\varepsilon$  and the permeability  $\mu$  such that

$$v = \frac{1}{\sqrt{\mu\varepsilon}}. \quad (2.14)$$

The phase velocity of an electromagnetic field in free space (i.e. vacuum) is, the speed of light

$$c = \frac{1}{\sqrt{\mu_0\varepsilon_0}} = 299,792,458 \text{ m/s}. \quad (2.15)$$

Whereas in a medium (i.e. optical fiber), the phase velocity is given by  $v = c/n$  where

$$n = \sqrt{\frac{\mu\varepsilon}{\mu_0\varepsilon_0}}. \quad (2.16)$$

In the case of optical fiber, the transparent Silica medium is nonmagnetic and therefore has a magnetic permeability  $\mu_0$ . In this case, the index of refraction now becomes  $n = \sqrt{\varepsilon/\varepsilon_0}$ . In nonmagnetic materials where  $\mu = \mu_0$ ,  $\varepsilon$  and therefore  $n$  become functions of the frequency  $\omega$ . The nature of the electromagnetic field vector and its requirement to satisfy Maxwell's equations in a charge-free, homogenous medium causes  $\vec{E}$  and  $\vec{H}$  to be perpendicular to the direction of propagation. For this reason, electromagnetic waves are said to be transverse waves. The transverse condition holds for all four field vectors of the plane wave in homogenous and isotropic media.  $\vec{E}$  and  $\vec{H}$  are in phase and in constant ratio provided  $\varepsilon$  and  $\mu$  are real.

### 2.2.3 Polarization

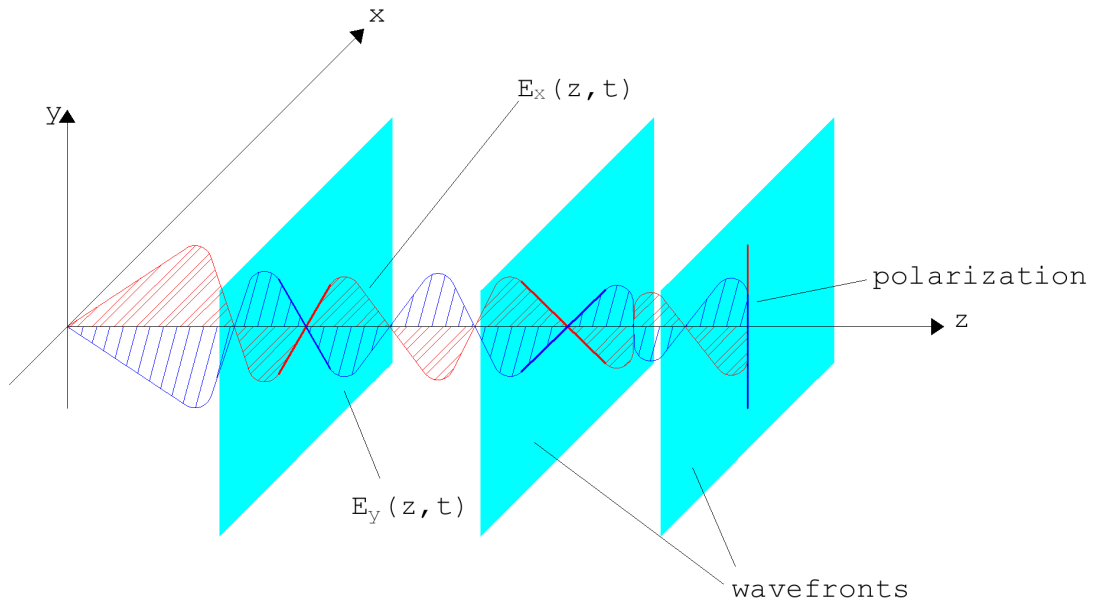
Consider a beam of light traveling through space in the direction  $+z$ . The beam is actually a set of oscillating electromagnetic waves traveling in the  $+z$  direction as shown in figure 2.4(a).

This field,  $E_x(z, t)$ , that is traveling in a homogenous, isotropic medium must have its transverse waves perpendicular to  $+z$  in order to satisfy Maxwell's equations for the plane wave solution. We can express the two mutually independent, transverse waves pictured in figure 2.4(b) in wave equation form as

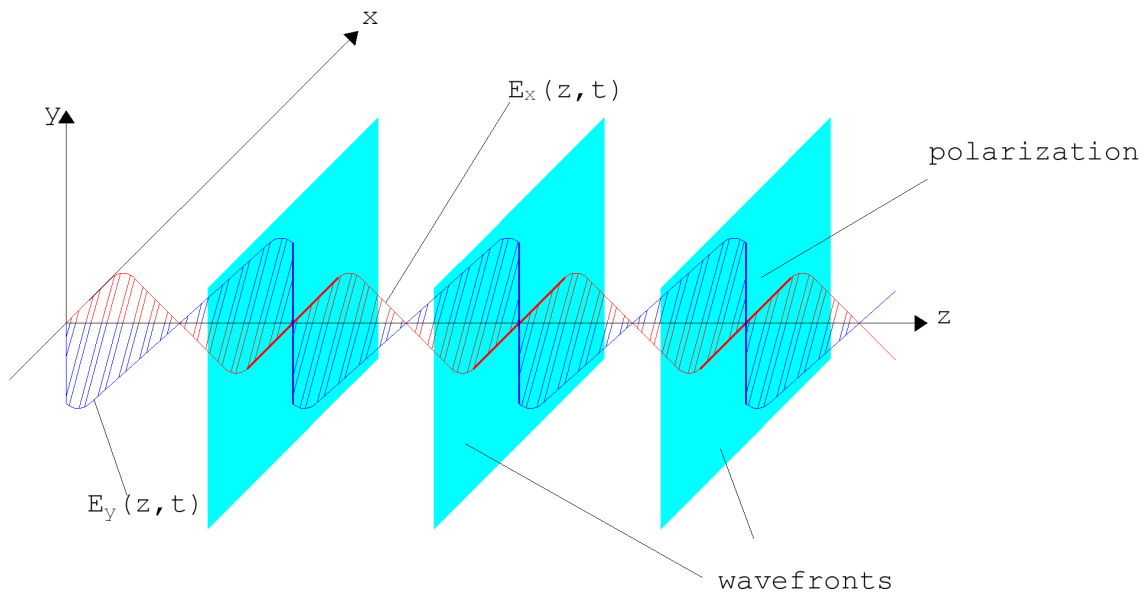
$$\begin{aligned} E_x &= A_x \cos(\omega t - kz + \delta_x) \\ E_y &= A_y \cos(\omega t - kz + \delta_y) \end{aligned} \tag{2.17}$$

where,  $A_x, A_y, \delta_x, \delta_y$  are the independent, positive amplitudes, and phase of the  $x$  and  $y$  components. Polarization refers to the orientation of the transverse oscillation in a waveguide [7]. The 2 mutually independent directions of oscillation,  $E_x$  and  $E_y$  are said to be *unpolarized* if there is no discernible correlation between the oscillations of the two transverse components as they travel through a medium, see 2.4(a). There are special cases of polarization in transverse wave, often known as *linear*, *elliptical*, or *circular*. This work





(a) Unpolarized



(b) Linearly Polarized

Figure 2.4: Polarization

concentrates on linear polarization, as shown in 2.4(b). The set of transversal waves are said to be linearly polarized if the components  $E_x$ ,  $E_y$  phases are in phase.

## 2.2.4 Guided Waves

As a beam of light travels through free space the transverse waves and all the difference directions or propagation *modes* will diverge and eventually spread. The modes contained in a medium can be called *guided modes*. Material and structures used to guide these electromagnetic modes are known as waveguides, the simplest being a dielectric slab waveguide [9]. In a homogenous dielectric medium, all components of an electromagnetic wave are continuous functions of time and space. When the wave components reach an abrupt change in the material properties (i.e.  $\epsilon$  and  $\mu$ ) the transversal fields of  $\vec{E}$  and  $\vec{H}$  are continuous across the interface [8]. This does not hold true is not true for the fields  $\vec{E}$  and  $\vec{H}$  normal to the interface.

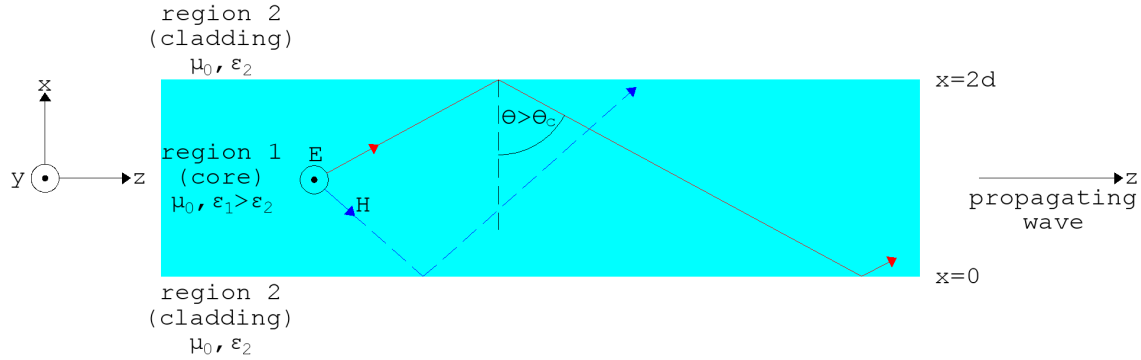


Figure 2.5: Dielectric slab waveguide

The solutions to Maxwell's equations must be calculated for each material then matched at the boundaries to ensure continuity. As a light ray crosses a change of medium, the light ray is reflected at an angle equal to the angle of incidence  $\theta_I$  with respect to the interface normal, as such  $\theta_I = \theta_R$ . Snell's law describes the angle at which the transmitted ray  $\theta_T$  enters the new material

$$\frac{\sin\theta_T}{\sin\theta_I} = \frac{n_1}{n_2}. \quad (2.18)$$

If the refractive index of the material the ray is leaving is less than the refractive index of the material the ray is entering  $n_1 < n_2$ , the angle of refraction  $\theta_T$  will be less than

the angle of incidence. The transmitted ray is bent towards the normal when the ray is traveling from a material having a lower refractive index. The opposite is true for a ray traveling from a material with index of refraction  $n_1$  greater than the index of refraction  $n_2$  of the new medium. The angle of the refracted ray is bent away from the normal.

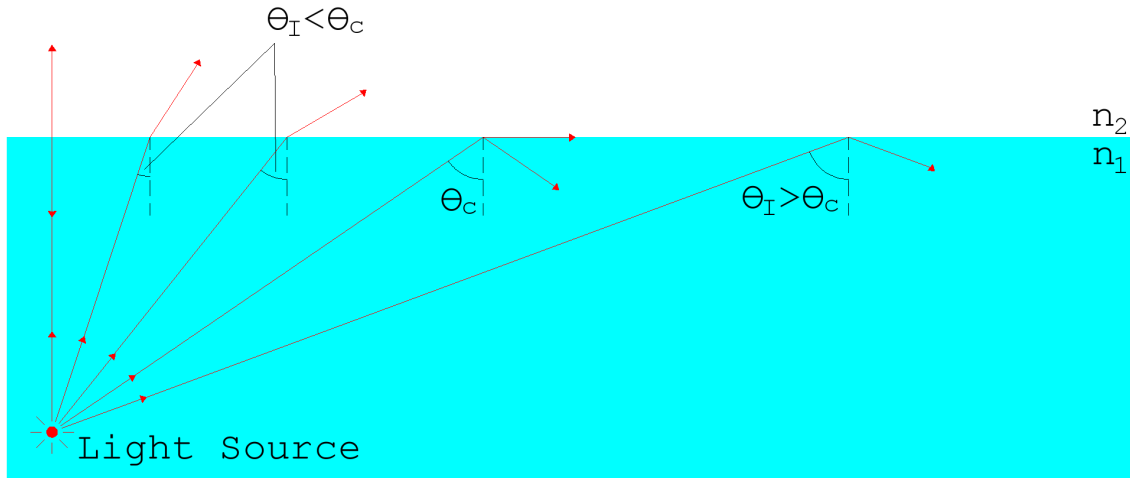


Figure 2.6: Snell's Law and Total Internal Reflection

Snell's law indicates that transmission cannot take place when the angle of incidence, in reference to the surface normal, is too large. Light cannot escape the material boundary if the angle of incidence and the refractive indices make the sine of the angle of transmission  $\theta_T$  equal to 1.0, as this makes the angle of the refracted ray  $90^\circ$ , and the light travels along the boundary. The incidence angle that produces this internal reflection is called the *critical angle*. Light rays entering an optical fiber core at or below the critical angle are trapped in the core experiencing little attenuation as they travel along the length of the core.

### 2.2.5 Single-mode Optical Fiber

An optical fiber is a thin,  $125\mu m$ , flexible, transparent medium that's capable of guiding light. Optical fiber is typically made from silica glass, has a cylindrical shape and consists of two concentric sections referred to the core and the cladding. A single-mode (SM) fiber

core is typically 8 to  $9.5\mu m$  in diameter, while the cladding surrounding the core is  $125\mu m$  in diameter. The core and the cladding have slightly different indices of refraction produced by adding dopants to the silica like fluoride or other oxides such as  $B_2O_3$ ,  $GeO_2$ , or  $P_2O_5$  [10]. The difference in index of refraction at the interface between the core and the cladding trap light rays traveling through the core by total internal reflection. The geometry of the optical fiber described is such that only one mode can be supported in the core.

$$V = \frac{2\pi a}{\lambda} \sqrt{n_1^2 - n_2^2} \quad (2.19)$$

where  $a$  is the core radius,  $\lambda$  is the wavelength in vacuum,  $n_1$  is the maximum refractive index of the core,  $n_2$  is the refractive index of the homogeneous cladding. In reality, fiber modes partly propagate in the core and in the cladding. The effective index of a mode, lies between the refractive indices of the cladding and the core. This is known as the effective index  $n_{eff}$ .

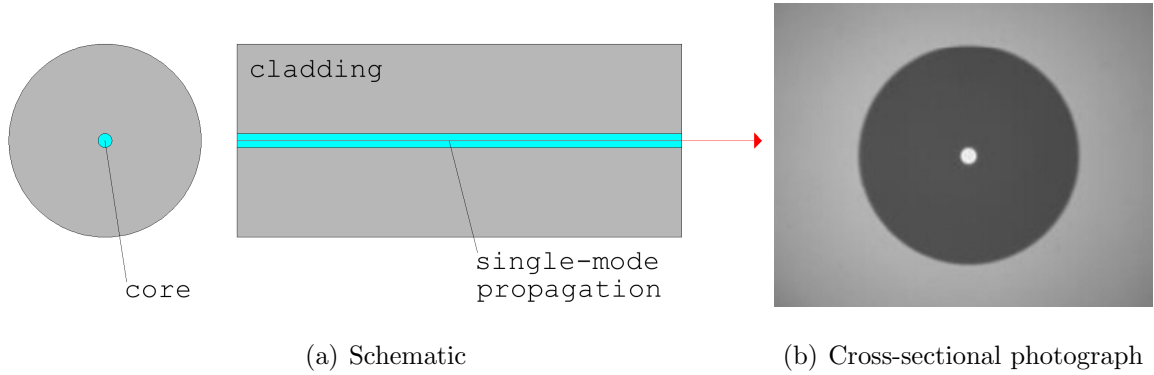


Figure 2.7: Single-mode optical fiber

### 2.2.6 Single-mode Polarization Maintaining Optical Fiber

In a SM fiber core of perfect circular symmetry, polarization would play no role in the transmission integrity of the light wave in the fiber. This however is never the case. Fiber cores are very seldom perfectly circular. More often than not, they are slightly elliptical. This induces what is known as stress induced optical birefringence. The index of refraction

is no longer the same throughout the cross-section of the core. Light waves traveling at different polarization orientations through the length of the SM core experience slightly different indices of refraction and therefore travel at different speeds, or wave velocities. This effect is called polarization mode dispersion [10]. Special fibers have been developed to control the polarization of light as it travels through the core. One such fiber, Polarization Maintaining single-mode (PM), has built in asymmetry in the core. Stress applying parts or rods (SAP) located in the cladding, induce a strain in the fiber core during the manufacturing process, resulting in an elliptical core, and the therefore birefringence. The induced birefringence, forces the coupled light wave polarization into the two extreme refractive index profiles, typically perpendicular to each other. These polarization directions are known as the fast and slow axis of the PM fiber.

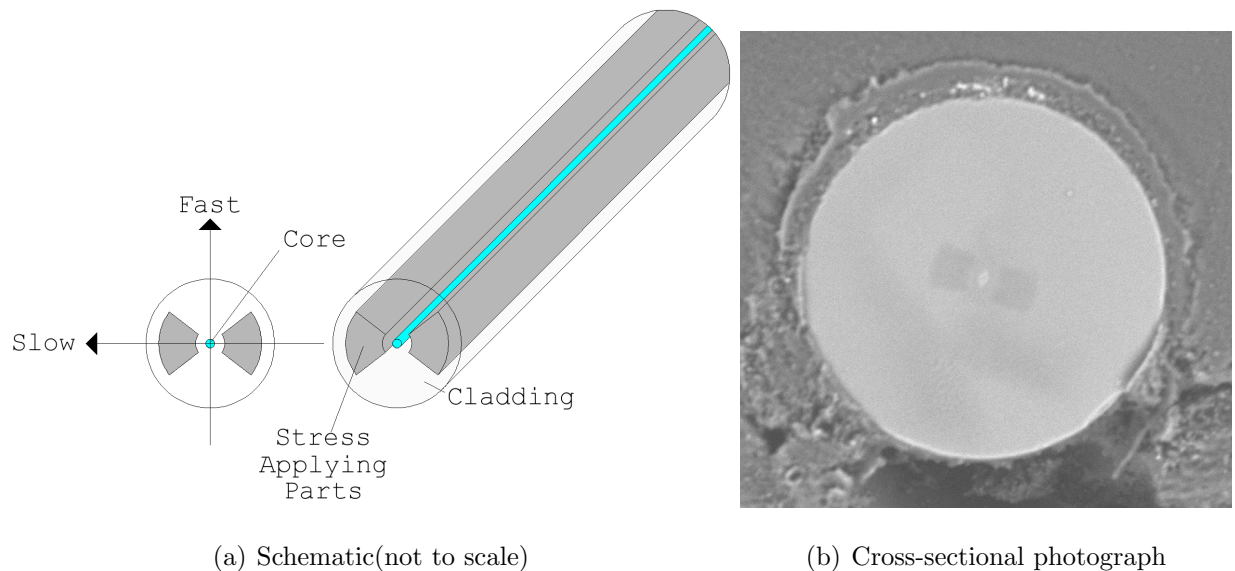


Figure 2.8: Polarization maintaining single-mode optical fiber

### 2.2.7 Fiber Bragg Gratings

A fiber Bragg grating (FBG) is a type of distributed Bragg reflector within a segment of an optical fiber. The structure is a periodic variation in the refractive index of the fiber core designed to reflect a specific set of wavelengths of light while transmitting all others.

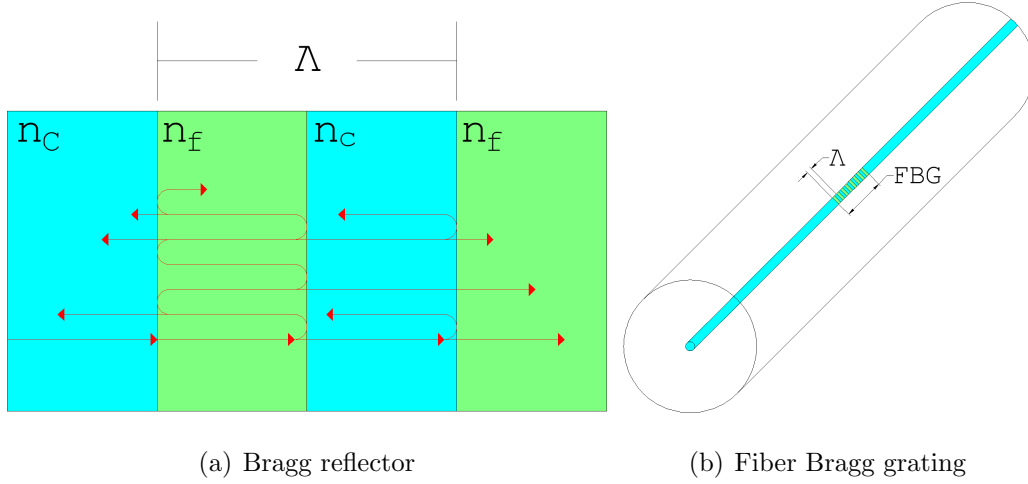


Figure 2.9: Fiber Bragg grating in single-mode optical fiber,  $n_c$  is the effective refractive index of the core, and  $n_f$  is that of the Bragg grating variation.

Each layer interface causes a partial reflection of the optical wave traveling with frequency  $\omega$ . The many reflections for each interface combine with constructive interference, ultimately blocking said frequency at the opposite end of the structure, while letting all others pass. As a whole the FBG acts like a dielectric mirror on the input end and a bandstop filter on the output end.

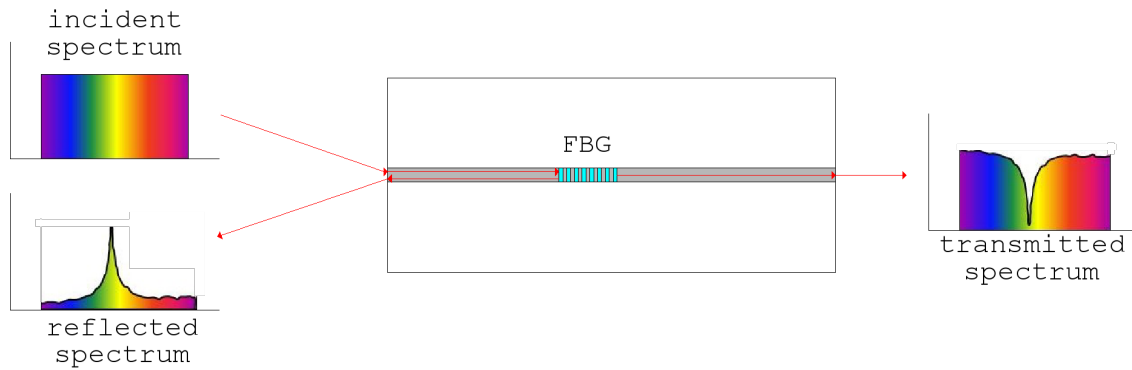


Figure 2.10: Fiber Bragg Grating Optical Response

The fundamental principle behind the behavior of an FBG in regards to the incident guided wave is defined by Fresnel's equations [12] for reflection and transmission [11]. In

a single-mode fiber, it is assumed there are at most, 2 guided modes propagating through the fiber core [10] by which the inference can be made that the incident, reflection and transmission angles  $\theta_c$  and  $\theta_f$  are very close to  $90^\circ$ . After every interface reflection and refraction, the incident wave continues to be confined within the waveguide.

$$r_{TE} = \frac{\sqrt{\frac{\mu_f}{\varepsilon_f}} \cos \theta_c - \sqrt{\frac{\mu_c}{\varepsilon_c}} \cos \theta_f}{\sqrt{\frac{\mu_f}{\varepsilon_f}} \cos \theta_c + \sqrt{\frac{\mu_c}{\varepsilon_c}} \cos \theta_f} \quad (2.20)$$

$$t_{TE} = 1 + R_{TE}$$

$$r_{TM} = \frac{\sqrt{\frac{\mu_g}{\varepsilon_g}} \cos \theta_g - \sqrt{\frac{\mu_c}{\varepsilon_c}} \cos \theta_c}{\sqrt{\frac{\mu_c}{\varepsilon_c}} \cos \theta_c + \sqrt{\frac{\mu_g}{\varepsilon_g}} \cos \theta_g} \quad (2.21)$$

$$1 + r_{TM} = \frac{\cos \theta_g}{\cos \theta_c} t_{TM}$$

The reflected wavelength ( $\lambda_B$ ), called the Bragg wavelength is defined by the reduced equation,

$$\lambda_B = 2n_g\Lambda \quad (2.22)$$

where  $n_g$  is the effective refractive index of the grating and  $\Lambda$  is the grating period. The wavelength spacing between the nulls, or the bandwidth  $\Delta\lambda$ , is given by,

$$\Delta\lambda = \left[ \frac{2\delta n_0 \eta}{\pi} \right] \lambda_B \quad (2.23)$$

It should be noted that multiple FBGs can be placed along the length of the fiber core, so long as the preceding FBG does not block the Bragg wavelength of the FBG after it, and so on.

## 2.3 Strain Analysis

The change in length and relative direction occasioned by deformation is called, loosely, strain. - Rankine, 1851.

In general terms, strain is a macroscopic measure of deformation. Applied forces or structure induce internal stresses which in turn produce deformations because real materials are not infinitely rigid. In short, mechanical strain is the mathematical expression of the shape changes resulting from mechanical stresses.

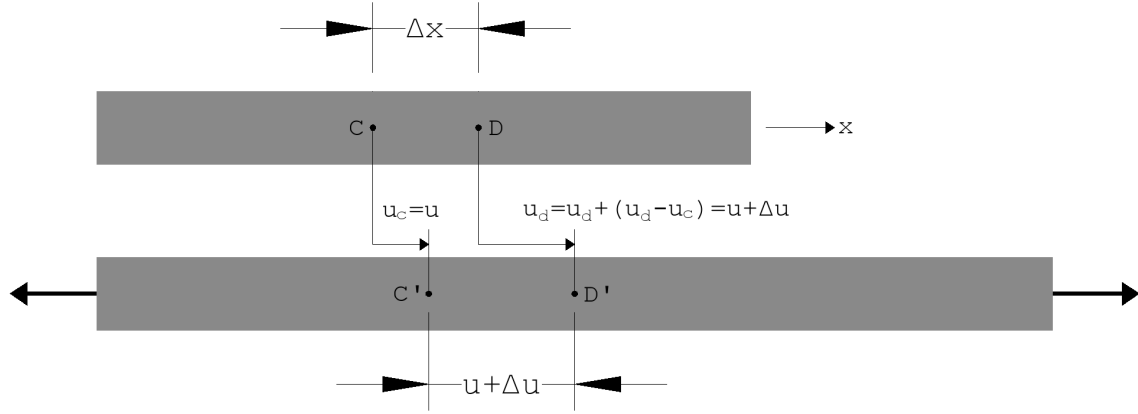


Figure 2.11: One-dimensional strain

Consider a bar with the long end oriented along the  $x$  axis. In the undeformed state, two points: C and D are separated by a small distance  $\Delta x$ , as shown in figure 2.2.3a. As the bar is pulled and moves to the deformed state, Figure 2.2.3b, points C and D move to positions C' and D', respectively. The point displacements along the  $x$  axis are  $u_C = u$  and  $u_D = u_C + (u_D - u_C) = u + \Delta u$ , respectively. The strain is obtained by taking the limit as  $\Delta = 0$  of the average strain over  $x$ . This relation between displacement and point-strains is called a strain-displacement equation [13].

$$\varepsilon_{xx} = \lim_{\Delta x \rightarrow 0} \frac{(u + \Delta u) - u}{\Delta x} = \frac{\Delta u}{\Delta x} = \frac{\partial u_x}{\partial x} \quad (2.24)$$



Instead of the bar, now consider a cube of finite size aligned with the  $x$ ,  $y$  and  $z$ , axes, as pictured in figure 2.3.

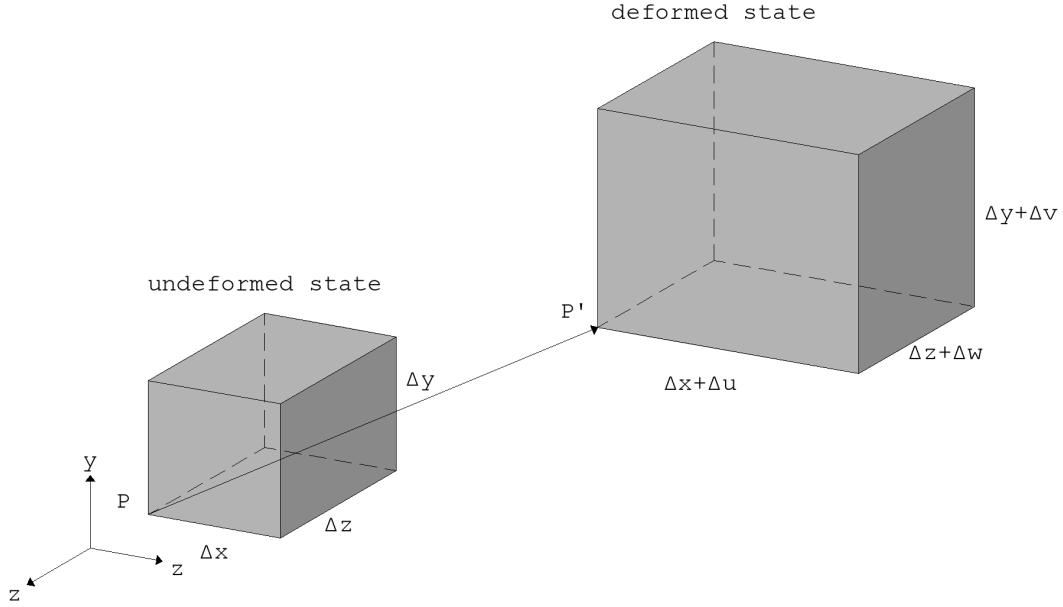


Figure 2.12: Undeformed and deformed cube of material in 3D. Shear strains are zero so angles are preserved. Displacement vector  $P P'$  has components  $u, v, w$  and  $x, y, z$ , respectively.

The cube has side dimensions  $\Delta x$ ,  $\Delta y$ ,  $\Delta z$  respectively, in the undeformed configuration. The cube in the deformed state has displacement components denoted by  $u$ ,  $v$ , and  $w$ , respectively. The deformed cube still remains a cube in the sense that after undergoing deformation, all the angles remain right angles. This is due to shear strains being zero. The side lengths however, change to  $\Delta x + \Delta u$ ,  $\Delta y + \Delta v$  and  $\Delta z + \Delta w$ , respectively. The averaged normal strain components are defined as

$$\begin{aligned}\epsilon_{xx} &= \frac{\Delta u}{\Delta x} = \frac{\partial u_x}{\partial x} \\ \epsilon_{yy} &= \frac{\Delta v}{\Delta y} = \frac{\partial u_y}{\partial y} \\ \epsilon_{zz} &= \frac{\Delta w}{\Delta z} = \frac{\partial u_z}{\partial z}\end{aligned}\tag{2.25}$$

The diagram illustrates the transformation of a rectangular element into a parallelogram element under a coordinate transformation. The left part shows a rectangular element with vertices A, B, C, D, width  $u_x(x, y)$ , height  $u_y(x, y)$ , and displacement  $u_y(x, y+dy)$ . The right part shows the transformed parallelogram element with vertices a, b, c, d, width  $u_x(x+dx, y)$ , height  $u_y(x, y)$ , and displacement  $u_y(x, y+dy)$ . The transformation is defined by the partial derivatives of the coordinates with respect to the original coordinates.

The shear strains  $\varepsilon_{xy}$ ,  $\varepsilon_{xz}$ , and  $\varepsilon_{yz}$  at point P are due to the partial-derivative sums

This expressions do not change if  $x$  and  $y$  are reversed, therefore  $\varepsilon_{xy} = \varepsilon_{yx}$ . We can

take the angles formed by planes  $(y, z)$  and  $(z, x)$  to define  $\varepsilon_{yz}$  and  $\varepsilon_{zx}$  as well. The property where  $\varepsilon_{xy} = \varepsilon_{yx}$ ,  $\varepsilon_{yz} = \varepsilon_{zy}$ , and  $\varepsilon_{zx} = \varepsilon_{xz}$ , is called shear strain reciprocity. It follows that the 3D state of strain at a point can be defined by 9 components: 3 extensional and 6 shear, which can be arranged as a  $3 \times 3$  matrix. On account of the shear strain reciprocity property, the above matrix is symmetric. Therefore it can be defined by 6 independent components: three normal strains and three shear strains [15].

$$\bar{\varepsilon} = \begin{bmatrix} \varepsilon_{xx} & \varepsilon_{xy} & \varepsilon_{xz} \\ \varepsilon_{yx} & \varepsilon_{yy} & \varepsilon_{yz} \\ \varepsilon_{zx} & \varepsilon_{zy} & \varepsilon_{zz} \end{bmatrix} \quad (2.27)$$

Strains are defined as the ratios of displacements divided by reference lengths. For normal strains, the usual observation is that extension in one direction is accompanied by a contraction in a transverse direction, this usually involves a volume change. In contrast, shear deformation is a change of shape with constant volume. If there is an increase in length of the material line, the normal strain is called tensile strain, otherwise, if there is reduction or compression in the length, it is called compressive strain. The normal strain is positive if the material fibers are stretched and negative if they are compressed. Measures of strain are unit-less and are often expressed in micro-strains  $\mu\varepsilon$  [14].

### 2.3.1 Strain Gauge

A strain gauge is a device used to measure strain on an object. Invented by Edward E. Simmons and Arthur C. Ruge in 1938, the most common type of strain gauge consists of a metallic foil pattern on an insulated, flexible backing. As the object is deformed, the foil is deformed, causing its electrical resistance to change. This resistance change, is related to the strain by the quantity known as the gauge factor [16]. When the electrical conductor is stretched, it will become narrower and longer, increasing its electrical resistance. Conversely, when a conductor is compressed it will broaden and shorten, decreasing its resistance measurement. A typical strain gauge arranges a long, thin conductive strip in a

zig-zag pattern of parallel lines such that a small amount of strain in the direction parallel to the foil lines, results in a larger strain measurement.

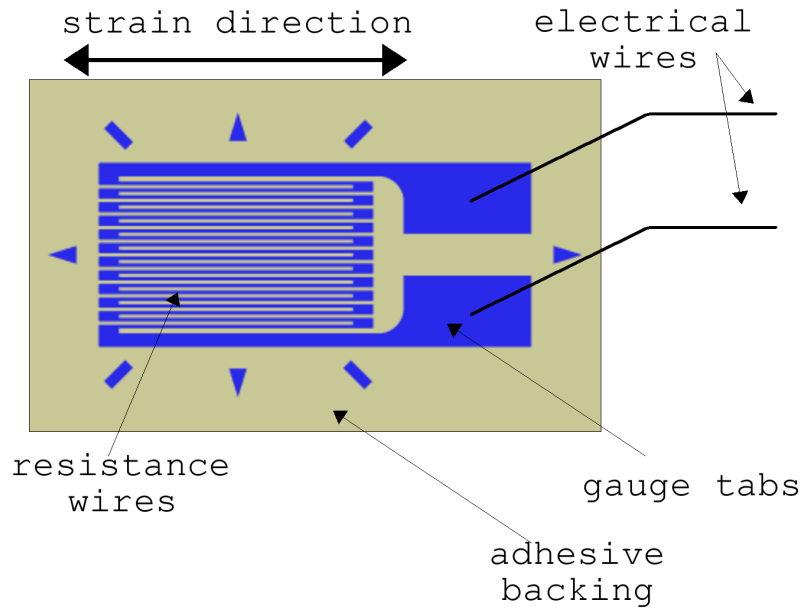


Figure 2.14: Foil resistive strain gauge

A wire strain gage can only measure strain in one direction. To determine the three independent components of plane strain, three strain measurements are needed, i.e., three strain gages or what is known as a strain gauge rosette.

Consider a strain rosette attached on the surface with an angle  $\alpha$  from the x-axis. The rosette itself contains three strain gages with the internal angles  $\beta$  and  $\delta$ . Suppose that the strain measured from these three strain gages are  $\varepsilon_a$ ,  $\varepsilon_b$ , and  $\varepsilon_c$ , respectively. The following coordinate transformation equation is used to convert the longitudinal strain from each strain gage into strain expressed in the pre-defined x-y coordinates.

### 2.3.2 Strain Transformation

Mohr's circle, named after Christian Otto Mohr, is a two-dimensional graphical representation of the transformation law for the engineering stress tensor. After performing a strain

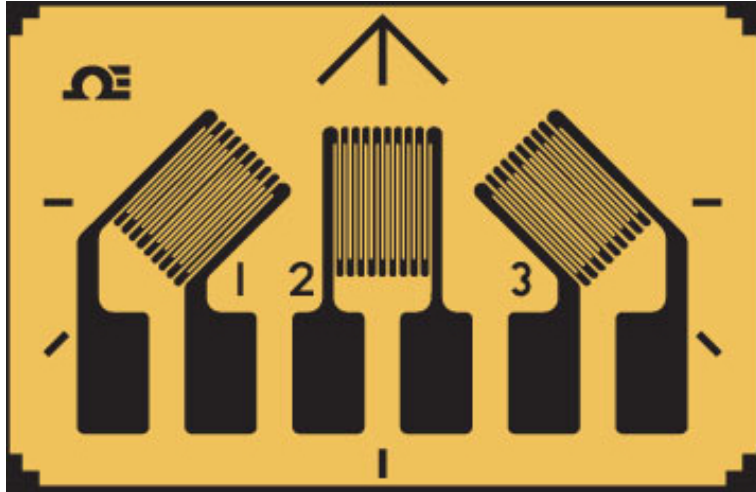


Figure 2.15: Strain gauge rosette

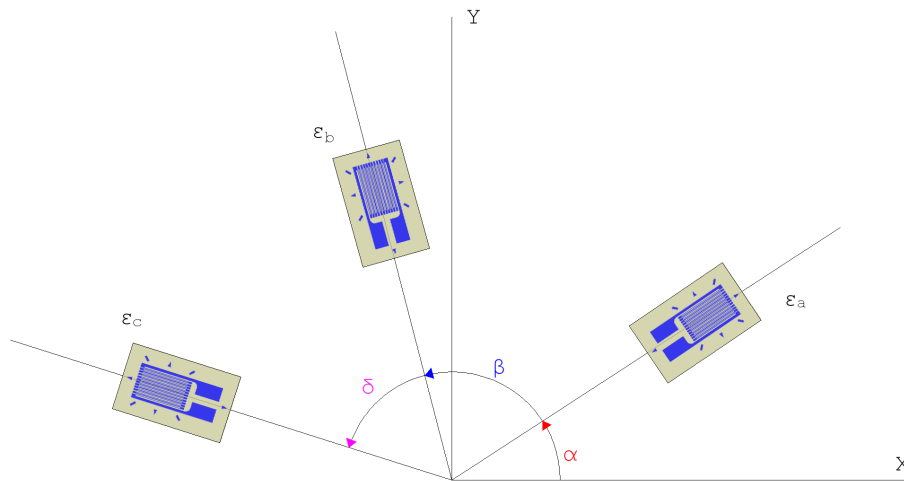


Figure 2.16: Rosette angles

analysis on a structure, the components of the strain tensor at a particular point on the structure are known with respect to a pre-defined coordinate system.

The Mohr circle is then used to determine graphically the stress components acting on a rotated coordinate system, i.e., acting on a differently oriented plane passing through that point.

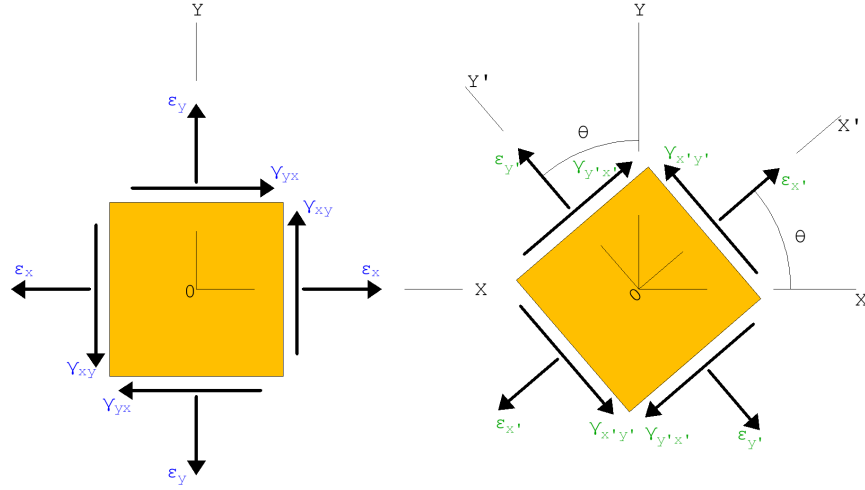


Figure 2.17: Strain axis transformation

$$\begin{aligned}
 \epsilon_x &= \frac{\epsilon_{x'} + \epsilon_{y'}}{2} + \frac{\epsilon_{x'} - \epsilon_{y'}}{2} \cos 2\theta - \frac{\epsilon_{x'y'}}{2} \sin 2\theta \\
 \epsilon_y &= \frac{\epsilon_{x'} - \epsilon_{y'}}{2} + \frac{\epsilon_{x'} + \epsilon_{y'}}{2} \cos 2\theta + \frac{\epsilon_{x'y'}}{2} \sin 2\theta \\
 \epsilon_{xy} &= \epsilon_{x'y'} \cos 2\theta + (\epsilon_{x'} - \epsilon_{y'}) \sin 2\theta
 \end{aligned} \tag{2.28}$$

# Chapter 3

## Mounted PM-FBG Sensor

In this chapter we explore the response of the PM-FBG optical sensor adhered to the surface of a test specimen subjected to uniaxial far field strains. This study is comprised of two experiments, a single PM-FBG and a two multiplexed PM-FBGs in a 0/45° rosette configuration. The purpose of the first experiment is validate past literature and derivations behind the strain/optic relationship. The first experiment will answer the following questions: How many strain elements in the strain tensor  $\varepsilon$  can be directly and indirectly measured with a single PM-FBG? What are the steps to accurately reconstruct the strain happening on the surface of the specimen? How accurate are these measurements compared to measurements given by uniaxial extensometer and DIC analysis? The second experiment extends the same test parameters to a two PM-FBG Rosette, with the expectation of reconstructing the full state of strain with in the rosette region.

In this chapter, the algorithm, shown in figure 3 for reconstructing a full state of strain at a point on the surface of a structure using PM-FBGs is derived. The following chapter applies this algorithm to 2 experiments: a single PM-FBG and rosette. Using the optical response and spacial information of the PM-FBGs, a full state of strain is, measured, calculated and validated.

### 3.1 Single PM-FBG

A single PM-FBG was adhered to the surface of a  $\frac{1}{4}$ " thick polycarbonate specimen as shown in figure 3.2(a). The adhesive is a two-part epoxy resin/polymercaptan and amine hardener. The mechanical properties of the epoxy adhesive and the PM-FBG sensor are

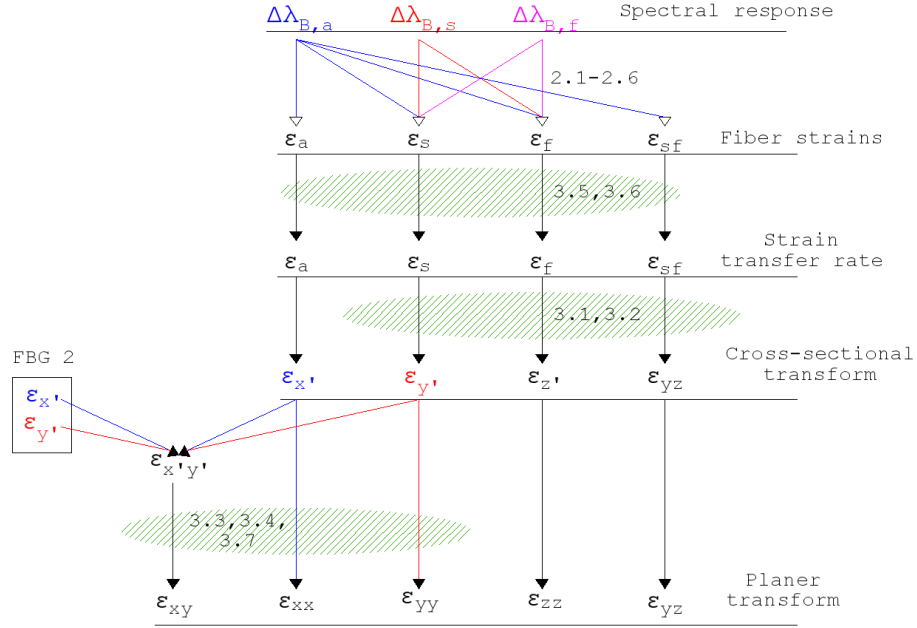


Figure 3.1: Strain evaluation algorithm

given in table 3.1.

Table 3.1: Single PM-FBG Material Properties

Materials Properties	Symbols	Values	Unit
Young's modulus, fiber	$E_f$	72	GPa
Poisson's ratio, fiber	$\nu_f$	0.17	–
Radius, fiber	$r_f$	62.5	$\mu\text{m}$
Young's modulus, epoxy	$E_e$	3.55	GPa
Poisson's ratio, epoxy	$\nu_e$	0.3	–
Radius, epoxy + fiber	$r_{ef}$	73	$\mu\text{m}$
Half length, FBG axial	$L_a$	6.5	mm
Half length, FBG cross-section	$L_{s,f}$	62.5	$\mu\text{m}$

The polycarbonate properties were omitted from the table, as they were unnecessary to calculate the strains from the specimen to the sensor. We are interested in reconstructing strains of the specimen, regardless of material composition, by comparing the spectral



behavior to the DIC and extensometer measurements. Polycarbonate was chosen as the test specimen due to its homogeneity and stress/strain linearity in the elastic region, allowing more precise characterization of the PM-FBG sensor itself.

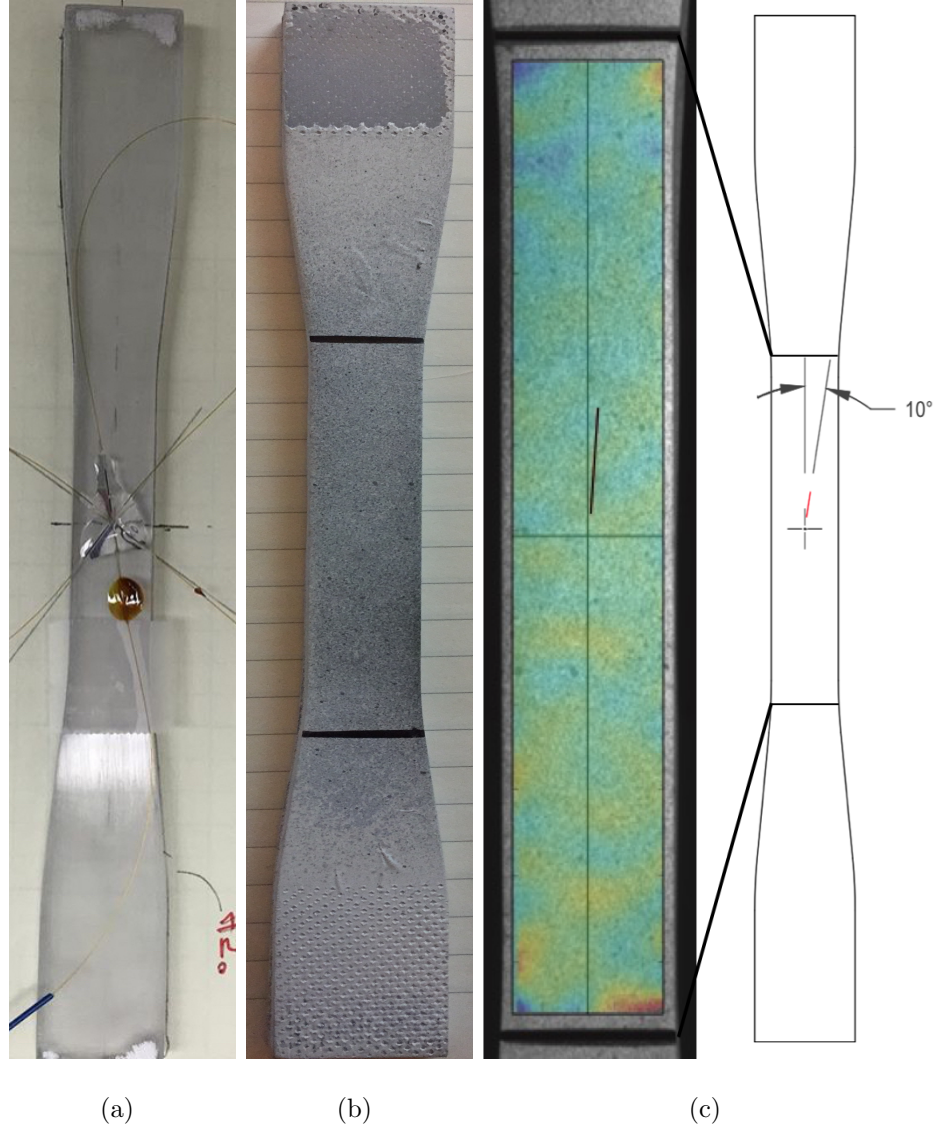


Figure 3.2: ASTM-D638 polycarbonate specimen with (a) PM-FBG adhered with epoxy, (b) DIC speckle pattern, (c) 50N  $\varepsilon_{yy}$  strain field with location of PM-FBG orientation of the fiber  $\varepsilon_a -10^\circ$  from primary axis strain  $\varepsilon_{yy}$

The opposite side of the specimen, figure 3.2(b) was speckled for two dimensional digital image correlation (DIC). The test specimen, with the PM-FBG attached underwent a single tension cycle from 0 - 2000N. The applied load is of continuous tension of the specimen with pauses at 5, 20, 50, 100, 150, 250, 500, 1000, 1500, 2000N measured the by the Instron testing system. These pauses allowed for discrete DIC camera snapshots and PM-FBG optical recordings.

### 3.1.1 Optical Interrogation

Linearly polarized, broadband light must be coupled into both polarization axes simultaneously to interrogate the sensor response to strain in both the slow and fast axes. Light from the Superluminescent diode (SLD) is split into two manual fiber polarization controllers. One is tuned for linearly polarized light coupling to the fast axis, the other coupled to the slow axis. The orthogonally polarized light is then combined into a single polarization maintaining fiber with the use of the a fiber-based polarization beam combiner. The circulator serves to reroute the reflected Bragg peak to the interrogator, blocking all other incoming signals from the SLD light source.

All optical components using PM fiber have the slow axis of mechanically aligned to the key of the FC/APC optical connectors. The optical response to strain for the fast and slow axis were recorded separately by disconnecting the output of the polarization controllers. The following procedure would occur for each force measurement: Run the mechanical tension movement, pause tension movement at the pre-defined force marker, take the DIC snapshot, disconnect the slow axis fiber optic link, take the fast axis optical snapshot, re-connect the slow axis link, disconnect fast axis link, take the optical snapshot, re-connect fast axis link, then commence the tension movement.

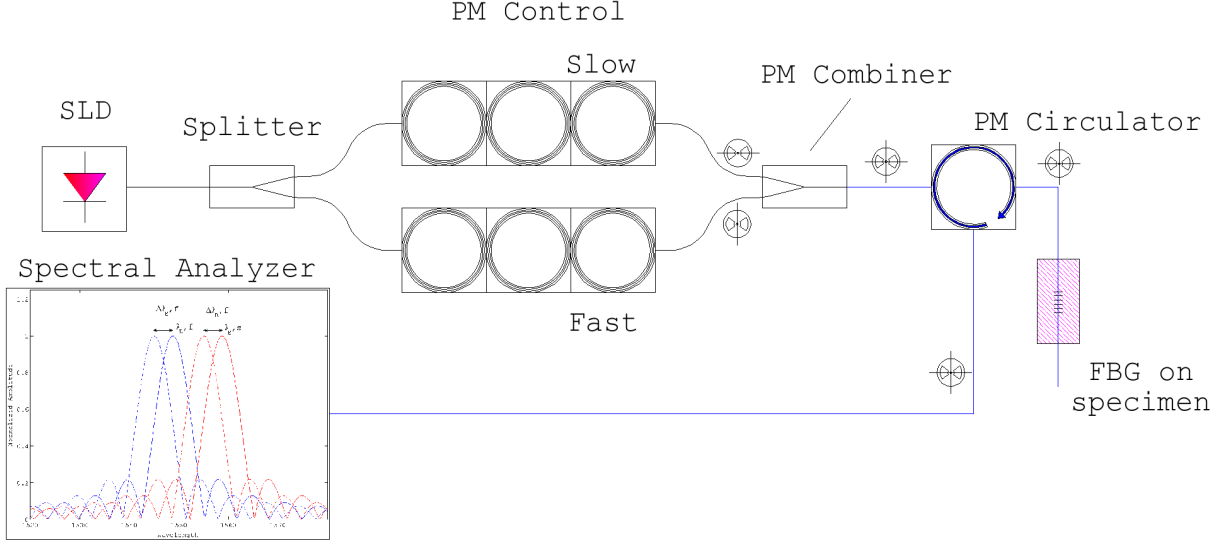


Figure 3.3: Optical test bench

### 3.1.2 Strain Transformations

Due to the cylindrical nature of the fiber optic sensor, the orientation of the slow and fast polarization axes with respect to the host structure must be known [30]. Ideally, the slow and fast axes of the PM fiber are aligned parallel or perpendicular, respectively, to the host plane. To our knowledge, there is no reliable, repeatable process to accurately embed or attach PM fiber sensors with a polarization axis aligned to a specific rotational orientation. That being said, knowing the angle  $\varphi$  of the slow polarization axes with respect to the host surface, the strains in the  $\varepsilon_s$  and  $\varepsilon_f$  plane can be transformed to the  $xz$  plane using Mohr's circle relation.

$$\begin{aligned}\varepsilon_{y'} &= \frac{\varepsilon_s + \varepsilon_f}{2} + \frac{\varepsilon_s - \varepsilon_f}{2} \cos 2\phi - \frac{\varepsilon_{sf}}{2} \sin 2\phi \\ \varepsilon_z &= \frac{\varepsilon_s + \varepsilon_f}{2} - \frac{\varepsilon_s - \varepsilon_f}{2} \cos 2\phi + \frac{\varepsilon_{sf}}{2} \sin 2\phi\end{aligned}\tag{3.1}$$

$$\varepsilon_{yz} = \varepsilon_{sf} \cos 2\phi + (\varepsilon_s - \varepsilon_f) \sin 2\phi\tag{3.2}$$

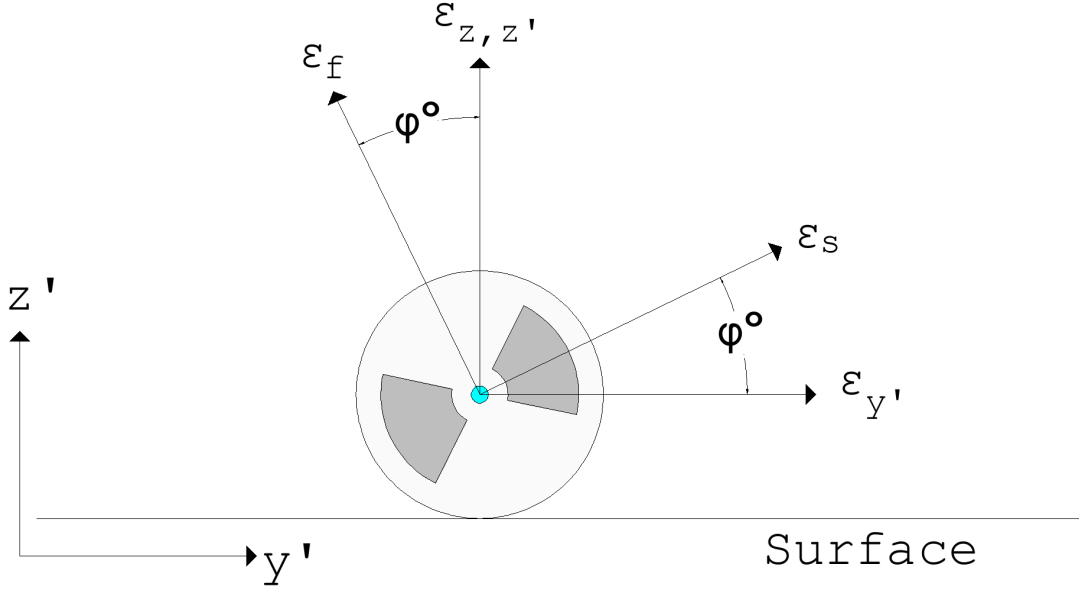


Figure 3.4: External strains  $\varepsilon_{y'}$  and  $\varepsilon_{z'}$  on the cross section of a PM optical fiber with  $\phi^\circ$  between the slow axis and the surface plane

The angle  $\varphi$  is considered positive in the counter-clockwise direction. At this point in the analysis,  $\varepsilon_{z'}$  can now be considered the principle strain  $\varepsilon_{zz}$ , which is the direction normal to the surface of the structure. Conversely,  $\varepsilon_{y'}$  is the strain measurement parallel to the surface of the host, but not necessarily aligned to any of the planar principle strain directions  $\varepsilon_x$  or  $\varepsilon_y$ . Therefore, along with  $\varepsilon_a$ ,  $\varepsilon_{y'}$  must undergo yet another strain transformation, this time with respect to the planar primary axis  $x$  and  $y$ .

The previously aligned slow  $\varepsilon_{y'}$  and measured axial  $\varepsilon_a$  strains of the PM-FBG sensor form what can be considered a 0/90 bi-axial stacked strain gauge rosette. Transforming the strains of  $\varepsilon_a$  and  $\varepsilon_{y'}$  to the host primary strain directions  $\varepsilon_x$  and  $\varepsilon_y$  respectively, can be done, again, through Mohr's circle relation.

$$\begin{aligned}
\varepsilon_a &= \varepsilon_{x'} \\
\varepsilon_x &= \frac{\varepsilon_{x'} + \varepsilon_{y'}}{2} + \frac{\varepsilon_{x'} - \varepsilon_{y'}}{2} \cos 2\theta - \frac{\varepsilon_{x'y'}}{2} \sin 2\theta \\
\varepsilon_y &= \frac{\varepsilon_{x'} - \varepsilon_{y'}}{2} + \frac{\varepsilon_{x'} + \varepsilon_{y'}}{2} \cos 2\theta + \frac{\varepsilon_{x'y'}}{2} \sin 2\theta
\end{aligned} \tag{3.3}$$

$$\varepsilon_{xy} = \varepsilon_{x'y'} \cos 2\theta + (\varepsilon_{x'} - \varepsilon_{y'}) \sin 2\theta \tag{3.4}$$

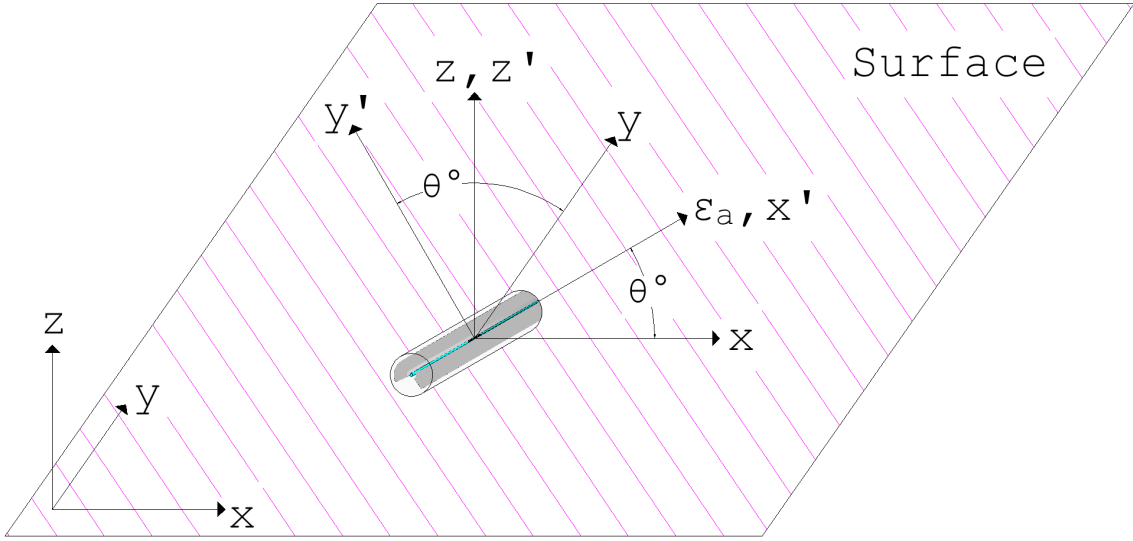


Figure 3.5: PM-FBG sensor with its axial  $\varepsilon_a$  and parallel to surface slow  $\varepsilon_s$  axes, placed on  $\theta^\circ$  and  $\theta^\circ + 90^\circ$  from the external principle strains  $\varepsilon_{xx}$  and  $\varepsilon_{yy}$  respectively

It is important to note, the geometry of the PM-FBG sensor does not allow it to measure shear strain with respect to its longitudinal axis [38]. For this reason, in particular for this experiment, we consider  $\varepsilon_{x'y'} = 0$ . An assumption can be made that all the shears with respect to the axial direction of the fiber  $\varepsilon_{as}$  and  $\varepsilon_{af}$  are 0.

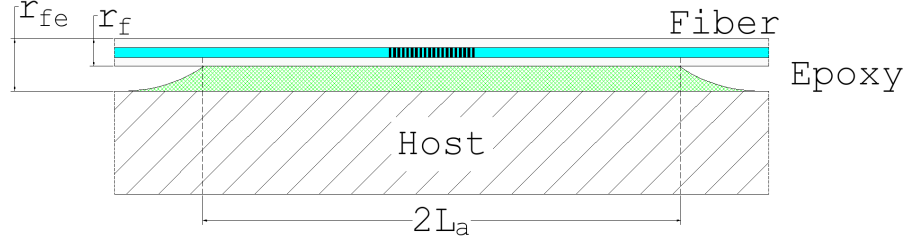
### 3.1.3 Strain Lag and Transfer Rate

When a FBG sensor is adhered to the surface of a host structure the magnitude of strain experienced by the host due to external loading, in any direction, is not the same as that experienced by sensor. This is in-part due to the differences in stiffness from the host material, through the adhesive on to the optical fiber [34]. The mathematical relationship used to account for the mis-alignment in material properties presented in this paper can be used given the following assumptions:

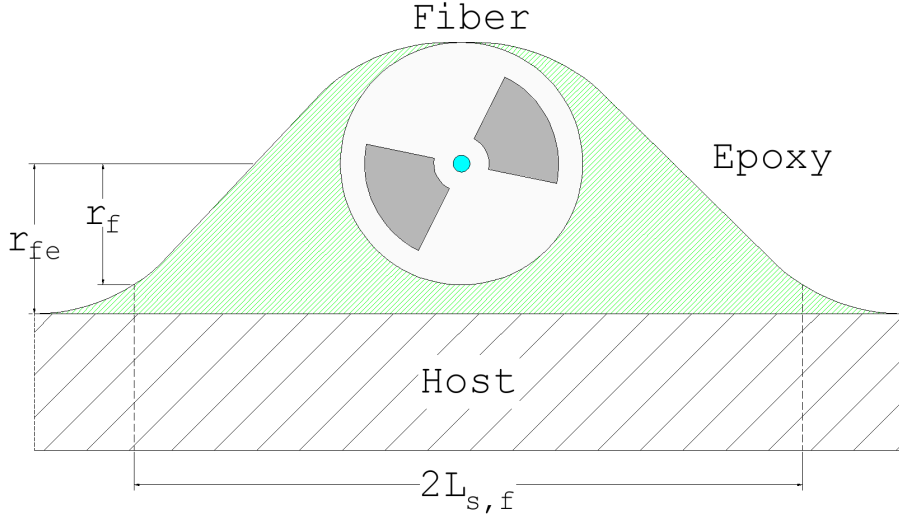
1. All the materials pertinent to the model remain elastic, and only the outer host material is subjected to axial stress and is uniformly strained, whereas the bare fiber and the adhesive layer do not directly bear any external loadings.
2. Mechanical properties of the core and cladding of the fiber are the same. In reality, their properties are slightly different owing to their difference in some chemical components and the writing process of Bragg gratings [28]. The core and cladding, hereinafter, are referred collectively as fiber.
3. There are no strain discontinuities across the interfaces, including the one between the host material and the adhesive layer and the one between adhesive layer and fiber interfaces, i.e., the bond between all the interfaces is perfect and no de-bonding exists.

The strain transferred from the host material to an optical fiber varies along the bond length of the fiber. The *Average* Strain Transfer Rate,  $\bar{\alpha}$  is defined as the ratio of the strains (in all directions, independently) on the PM-FBG to the actual strains on the structure over the length of the bonded region. Shown in derived form, equation 3.5 depends on the symmetrical half-length of the bond area  $L$  and the strain lag parameter  $k$  [36].

$$\bar{\alpha} = \frac{\varepsilon_{a,s,f}}{\varepsilon_{a_m,s_m,f_m}} = \left[ 1 - \frac{\sinh(kL)}{kL \cosh(kL)} \right]. \quad (3.5)$$



(a) Axial



(b) Transversal

Figure 3.6: Diagram of symmetrical sections for the fiber adhered by epoxy resin, axial and cross sectional views.

$$k = \sqrt{\frac{2G_e}{r_f^2 E_f \ln(\frac{r_{ef}}{r_f})}}. \quad (3.6)$$

$G_e = E_e/2(1 + \mu)$  is the shear modulus of the epoxy layer. Calculating  $\varepsilon_{a_m}$ , which refers to the host structure strain following the axial direction of the fiber, is a direct application of equations 3.5 and 3.6 per figure 3.6(a). To calculate the strain transfer rate in both  $\varepsilon_{s_m}$  and  $\varepsilon_{f_m}$  directions, we make the assumptions that the half bond length  $L_{s,f}$  is as shown in figure 3.6(b).

## 3.2 PM-FBG Rosette

Two independent, multiplexed PM-FBGs are adhered in a rosette pattern on the surface of the ASTM D638-Type1 polycarbonate specimen using the same two-part epoxy resin/polymercaptan and amine hardener adhesive specified in section 3.1. The opposite side of the specimen, again, was speckled for DIC analysis.

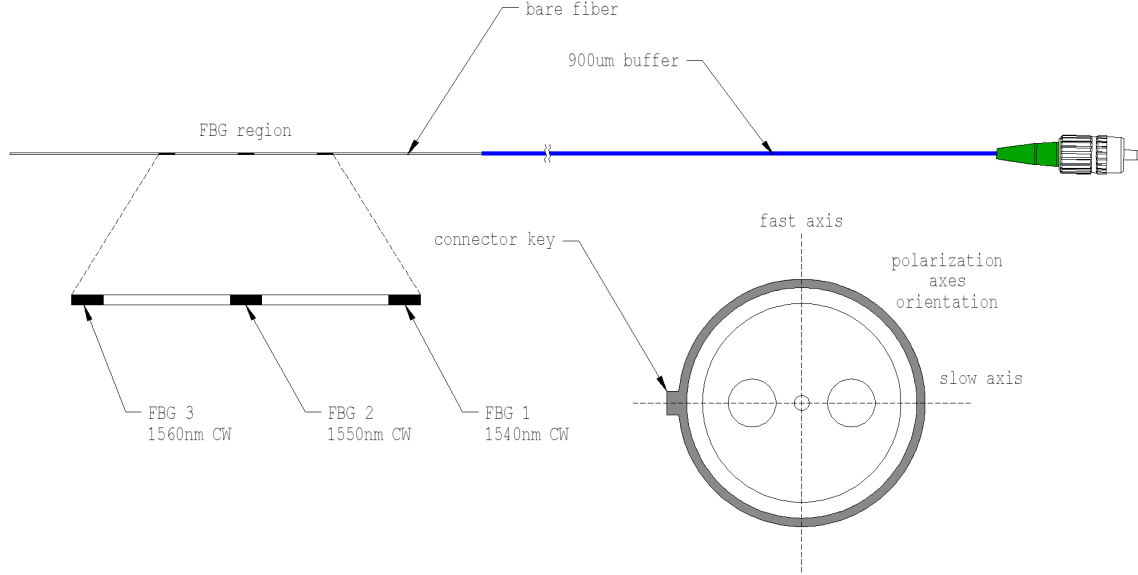


Figure 3.7: Three-FBG sensor in PM optical fiber

The two FBGs are written to the same PM core at different locations across the axial length of the fiber and are designed to reflect wavelengths centered at 1550 and 1560 nm. We denote these as FBG2 and FBG3, respectively. Each FBG has a length of 4mm as pictured in figure 3.2. The optical fiber pictured has a three multiplex FBGs, however only 2 sensors were mounted, leaving the FBG designed to reflect 1540nm intact for future use. The tension test parameters remained the same as with the single PM-FBG. All the same materials were used as per the pervious test, including the specimen and epoxy adhesive. It should be noted however, the manufacturer for the sensor rosette is different than the manufacturer of the single PM-FBG version. The most notable differences being the use



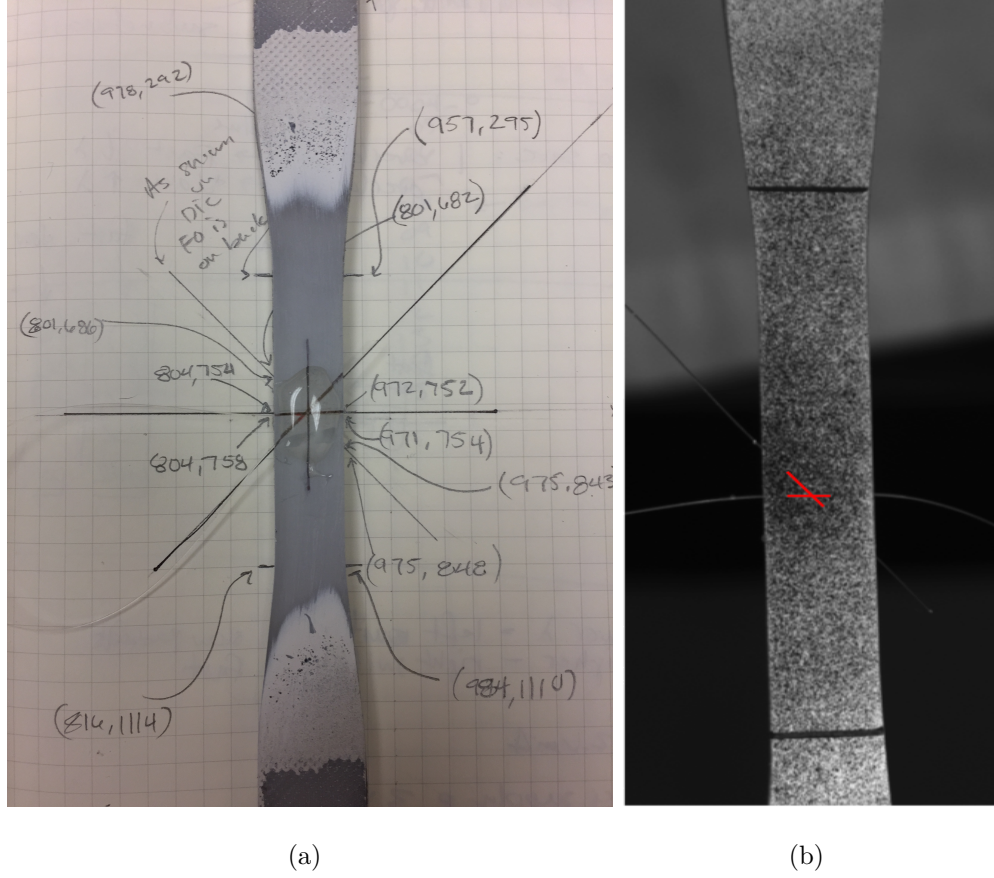


Figure 3.8: ASTM-D638 polycarbonate specimen with (a) PM-FBG adhered with epoxy, (b) DIC speckle pattern,

of PANDA PM fiber as opposed to Bow-Tie and the use of an Acrylate re-coating on the FBG region. The difference in the strain-to-optical response, or *gauge factor* from PANDA to Bow-tie PM fiber is negligible [39][30]. The FBG re-coat, however, is not [36].

### 3.2.1 Optical Interrogation

The optical interrogation system, in a quest to improve the integrity of the signal and simplify the capture procedure, underwent the following modifications:

1. Polarization filters were integrated at the output of each polarization controller, ensuring a better discrimination and amplitude control between the polarization directions.

2. A PM splitter was integrated after the PM circulator and before the optical switch. Designed to split on the basis of polarization it has an extinction ratio of over  $20dB$ .
3. A  $1 \times 2$  latching-style fiber optic switch was integrated at the input of the spectral analyzer. This switch eliminates the need to mechanically disconnect and reconnect the optical connectors in order to interrogate the two polarization axes independently.

### 3.2.2 Strain Transformations

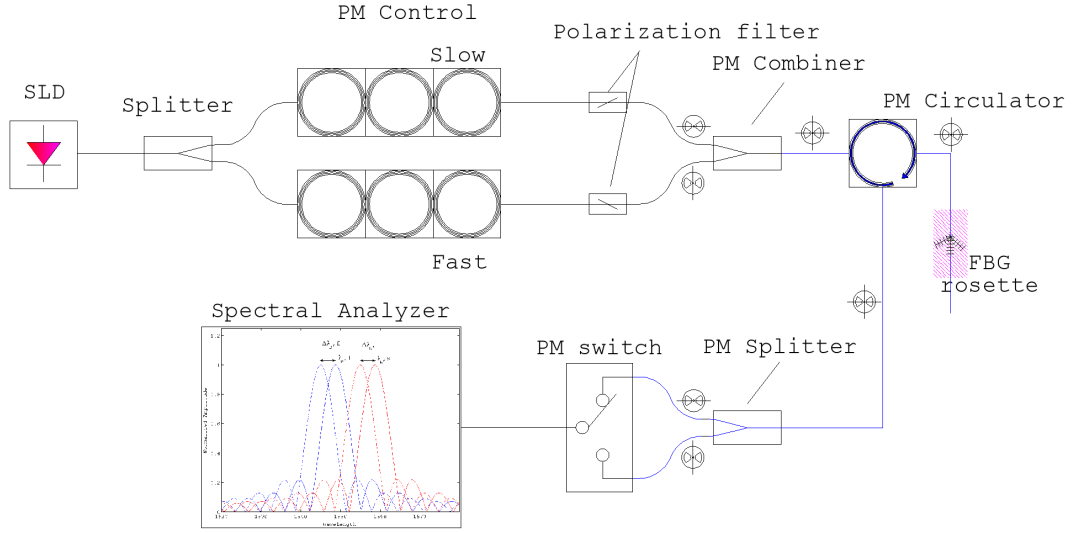
The equations 3.1 through 3.4 in section 3.1.2 the can be used transform the measured strain  $\varepsilon_a$ ,  $\varepsilon_f$  and  $\varepsilon_s$  of FBG2 and FBG3, to the primary  $\varepsilon_{xx}$ ,  $\varepsilon_{yy}$ ,  $\varepsilon_{zz}$  axes. The out-of-plane shear strain direction  $\varepsilon_{yz}$  for each sensor is calculated via equations 3.1 and 3.2 [22]. The simultaneous measurement axes  $\varepsilon_a$  and  $\varepsilon_s$  on a planar surface can be considered analogous to a conventional 0/90 bi-axial stacked strain gauge rosette. Two PM-FBGs that co-located within millimeters of each other, result in four simultaneous strain measurements in a single point.

The strain measurements from the co-located PM-FBGs can be used to calculate the planar shear strain  $\varepsilon_{xy}$  using equations

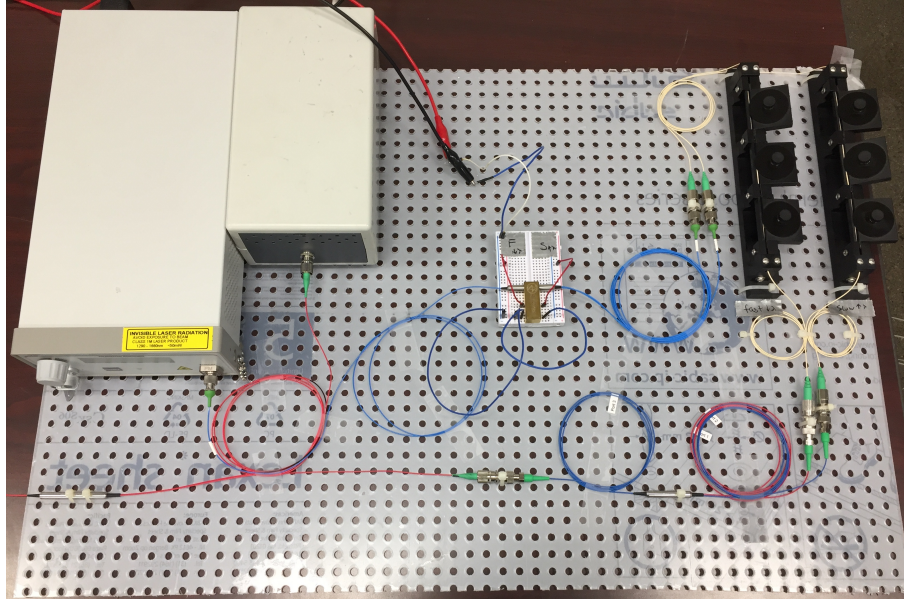
$$\begin{aligned}
\varepsilon_{xx} &= \varepsilon_{a2} \\
\varepsilon_{yy} &= \varepsilon_{s2} \\
\varepsilon_{xy} &= 2\left(\varepsilon_{s2} - \frac{\varepsilon_{a2} + \varepsilon_{as}}{2}\right).
\end{aligned} \tag{3.7}$$

### 3.2.3 Strain Lag and Transfer Rate

The same strain transfer rate described in section 3.1.3 was applied to each PM-FBG employing the values delineated in table 3.2.3. The figures 3.11(a) and 3.11(b) show the total radius for FBG2 and FBG3, respectively. This *total radius* is defined as the cross-sectional distance of the center of the FBG from the surface of the specimen embedded in



(a) schematic



(b) optical

Figure 3.9: Modified optical interrogation system

the epoxy. It is apparent that FBG2 and to a greater extent FBG3 are further from the specimen surface compared to the previous single PM-FBG experiment. Figures 3.11(a) and 3.11(b) also show the Acrylate re-coat around the FBG region, not present in the first experiment. The effects of the increased distance and coating are described in the

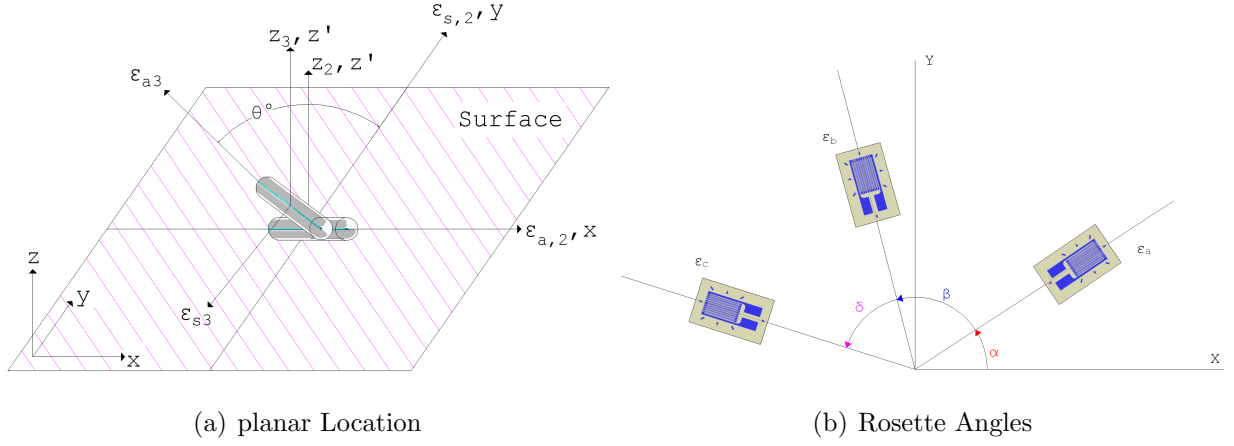
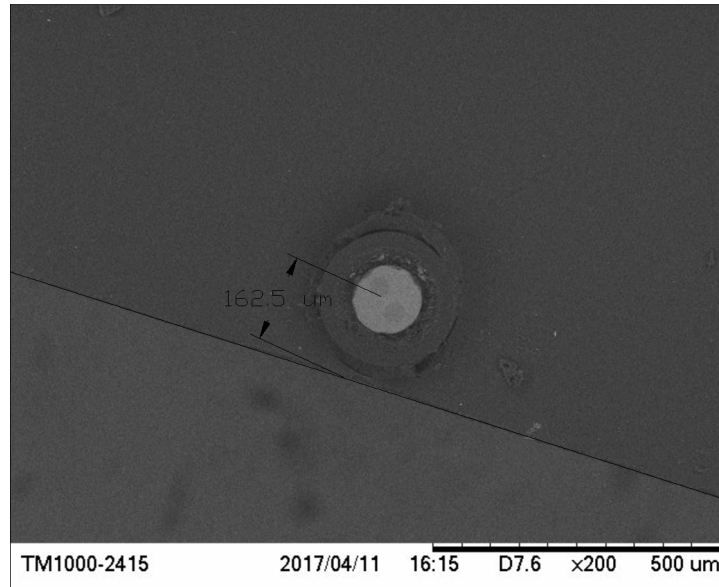


Figure 3.10: PM-FBG rosette location on strain field and gauge angles compared to XY axis

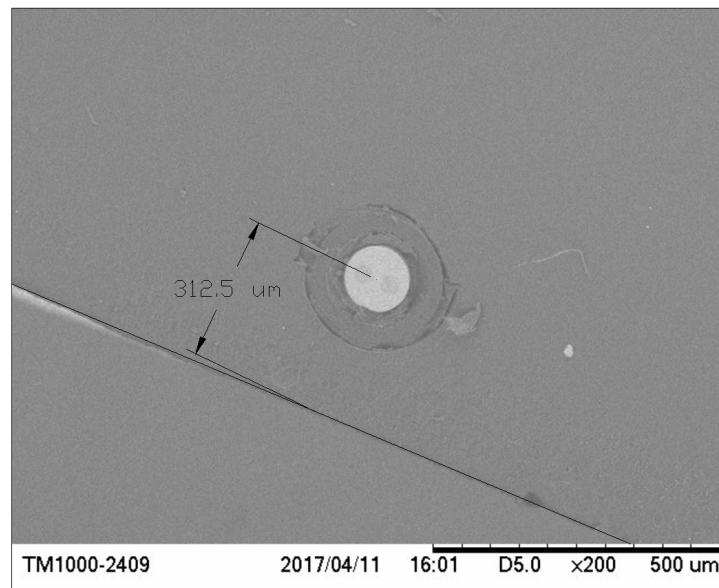
proceeding section.

Table 3.2: PM-FBG Rosette Material Properties

Materials Properties	Symbols	Values	Unit
Young's modulus, fiber	$E_f$	72	GPa
Poisson's ratio, fiber	$\nu_f$	0.17	—
Radius, fiber	$r_f$	62.5	$\mu\text{m}$
Young's modulus, epoxy	$E_e$	3.55	GPa
Poisson's ratio, epoxy	$\nu_e$	0.3	—
Radius, epoxy + FBG2	$r_{ef}$	162.5	$\mu\text{m}$
Radius, epoxy + FBG3	$r_{ef}$	312.5	$\mu\text{m}$
Half length, FBG axial	$L_a$	6.5	mm
Half length, FBG cross-section	$L_{s,f}$	62.5	$\mu\text{m}$



(a) FBG2



(b) FBG3

Figure 3.11: Cross section of FBG 2 and 3 showing distance of sensor to specimen surface.

# Chapter 4

## Experiment Results and Analysis

In this chapter, the transformed strain measurement from the single and rosette PM-FBG are compared to extensometer and DIC strain measurements of the test polycarbonate specimen. The two dimensional DIC and uniaxial extensometer are only able to measure planar states of strain e.g.  $\varepsilon_{xx}$ ,  $\varepsilon_{yy}$ , and  $\varepsilon_{xy}$ . Correlation, mean and percent errors per load measurement and standard deviation values are given for the two principle and shear comparisons. The other strain tensor elements contain out of plane components and cannot be compared at this time. However, since all principle strains and PM-FBG cross-sectional shears are needed to compute the full state of strain. The accuracy of  $\varepsilon_{xx}$ ,  $\varepsilon_{yy}$ , and  $\varepsilon_{xy}$  for PM-FBG can be assumed to hold true on the other elements due to the transformation relationships presented in Chapters 2 and 3.

### 4.1 Single PM-FBG

From the pre-determined sensor and host measurements, a digitized sensor location in reference to the DIC test grid was established. The PM-FBG itself is  $6mm$  in length. The FBG region is located at pixels  $[x = 871 ; y = 531]$  of the DIC reference. The length of the PM-FBG spans 125 pixels in the Y direction, and 10 pixels in the Y direction. A digital representation of the location of the PM-FBG on the specimen is displayed in figure 3.2(c). Figure 4.1 shows DIC images of the normal strain fields measured during the tensile test at 500N load.

When the vertical (y-axis) tensile force is increased, the host experienced an increase in positive strain  $\varepsilon_{yy}$  signifying tension in the y direction. Conversely, the we see a negative

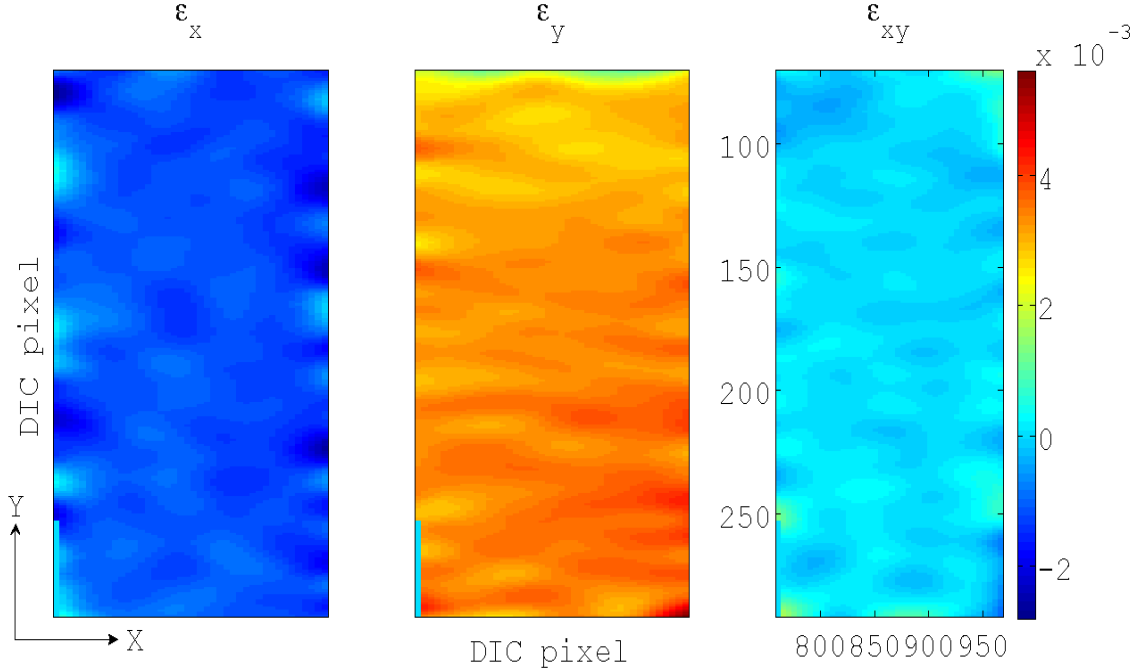
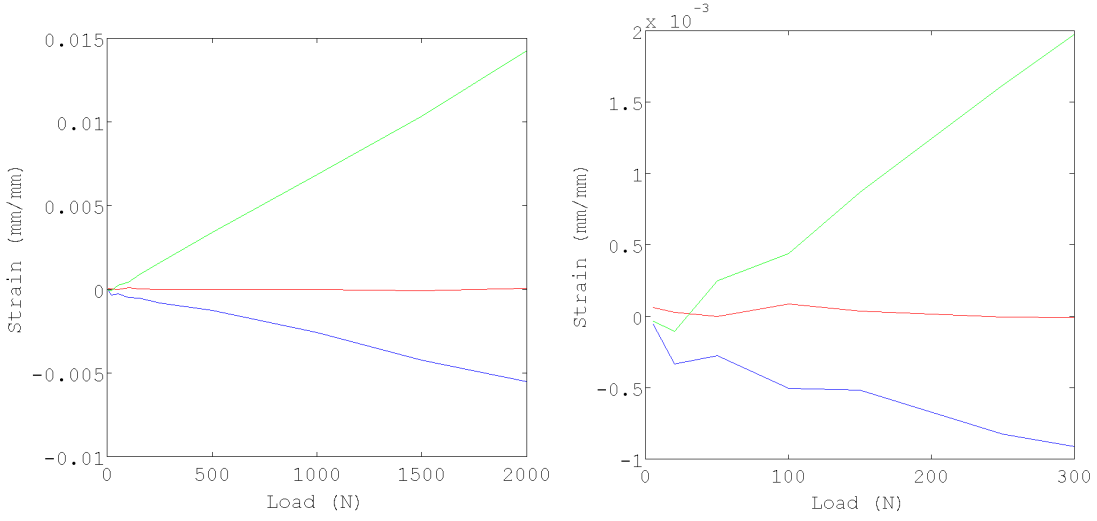


Figure 4.1: DIC measurements  $\varepsilon_x$  left,  $\varepsilon_y$  center,  $\varepsilon_{xy}$  right.

decrease in  $\varepsilon_{xx}$ , marking compression along x. This is evident in figures 4.2(a) and 4.2(b). Figure 4.2(c) is the  $\varepsilon_{yy}$  strain as measured by the uniaxial electronic extensometer.

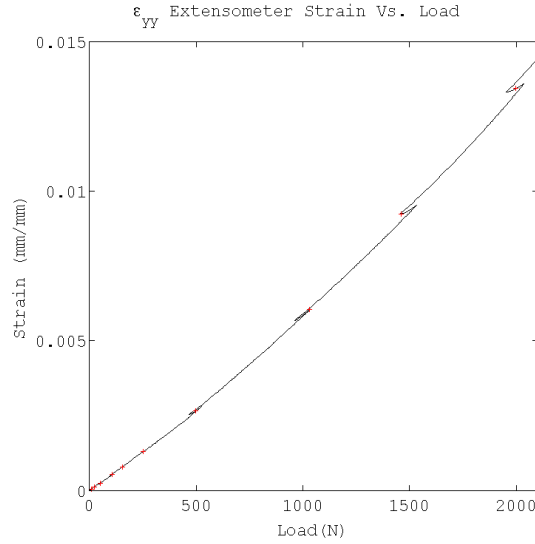
The optical response of the FBG sensor does indeed change with the increasing external force, the deltas in wavelength for  $\lambda_B$ ,  $\lambda_{Bs}$ , and  $\lambda_{Bf}$  were extracted using the method provided in [20] then applied to s 2.2 - 2.6. This results in the fiber optic strain measurements  $\varepsilon_a$ ,  $\varepsilon_s$ ,  $\varepsilon_f$  and  $\varepsilon_{sf}$ . We divide each strain element by  $\bar{\alpha}$ , the average strain rate, to obtain the strain values  $\varepsilon_{am}$ ,  $\varepsilon_{sm}$ ,  $\varepsilon_{fm}$ , and  $\varepsilon_{sfm}$ . At this point, we have the specimen strain as applied to the sensor through the epoxy adhesive, but not necessarily aligned to any structural axes, primary or otherwise. Proceeding the tensile test, the sensor and epoxy were removed from the specimen, cut, and polished to reveal its cross section and the orientation of the slow and fast axes in relation to the surface of the polycarbonate.

The cross-section and axial strain transformations are applied to the strains  $\varepsilon_{am}$ ,  $\varepsilon_{sm}$ , and  $\varepsilon_{fm}$  with the angle values the  $\varphi = -17^\circ$  and  $\theta = 80^\circ$  respectively, to obtain the strain measurement in the pre-defined primary directions  $\varepsilon_{xx}$ ,  $\varepsilon_{yy}$ , and  $\varepsilon_{zz}$ . The strain normal



(a) Full view

(b) 0 - 300N zoom



(c) Full view w/ discrete load points

Figure 4.2: DIC Strain,  $\epsilon_x$  (blue),  $\epsilon_{xy}$  (red),  $\epsilon_y$  (green), extensometer

to the surface of the host structure,  $\epsilon_{zz}$  is not reflected in the DIC measurements but was used in the analysis and is shown in figure 4.5(c) for reference.

Comparing the strain measured by the extensometer for the y-axis, DIC for the x and xy-shear axes to the PM-FBG measured strain, we see a strong Pearson linear correlation across all the finite load measurements of 0.98 and 0.99 for  $\epsilon_{xx}$  and  $\epsilon_{yy}$ , respectively. The planar



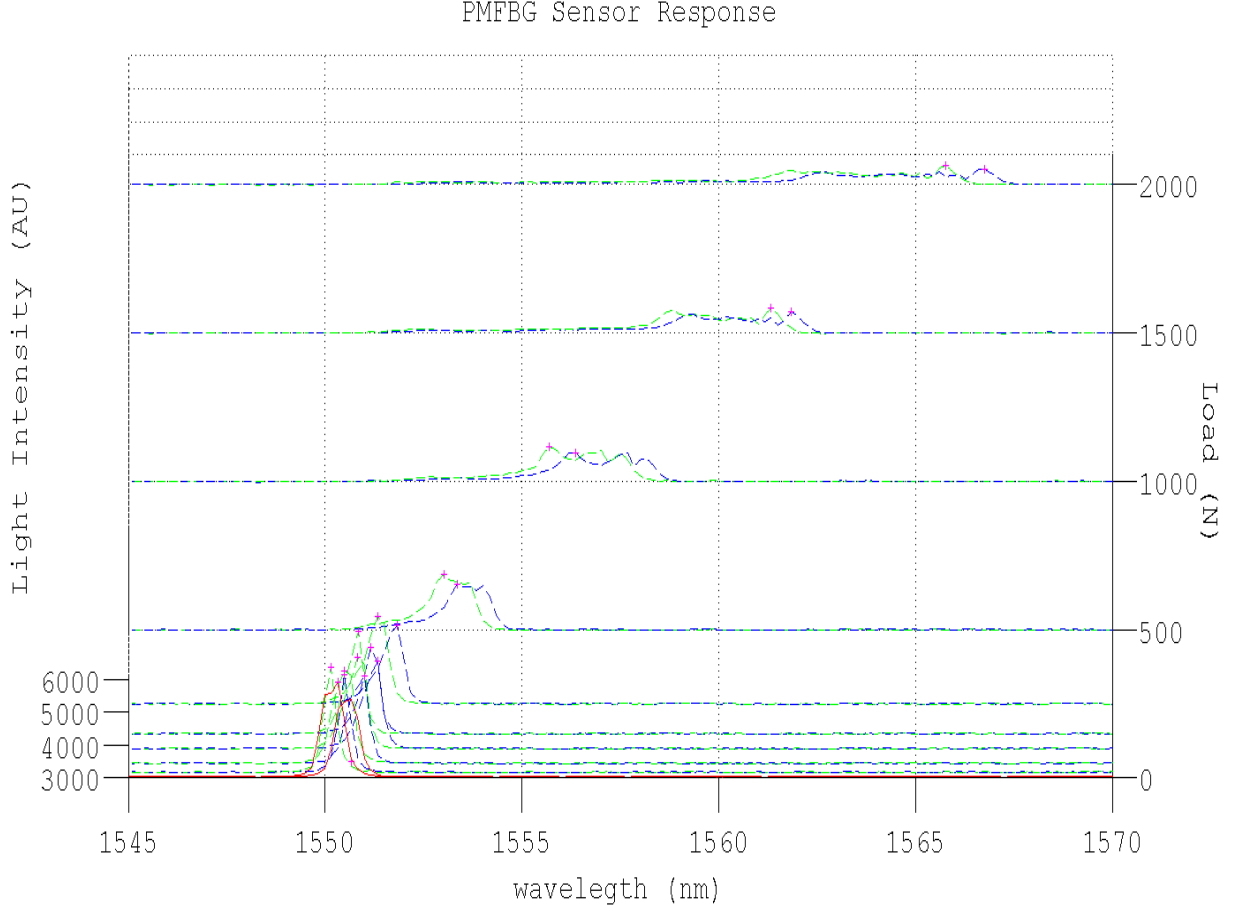


Figure 4.3: Mounted PM-FBG optical wavelength shift response at 5 - 2000 N specimen loads with fast green and slow blue axes.

shear strain  $\varepsilon_{xy}$  resulted in non-correlation, -0.27. The mean error, standard deviation and gauge factor for each sensing direction of the PM-FBG are listed in table 4.1.

Table 4.1: Single PM-FBG Sensor Measurement Error, Std. Deviation, % Error

Axis	Mean Error $\frac{mm}{mm}$	Std. Deviation $\frac{mm}{mm}$	Avg. Gauge Factor
$\varepsilon_{xx}$	$5.65 \times 10^{-4}$	$6.32 \times 10^{-4}$	0.403
$\varepsilon_{yy}$	$3.68 \times 10^{-4}$	$6.50 \times 10^{-4}$	-0.9262
$\varepsilon_{xy}$	$1.46 \times 10^{-4}$	$2.37 \times 10^{-4}$	-

For this particular test, an error was introduced in the strain measurement with the split

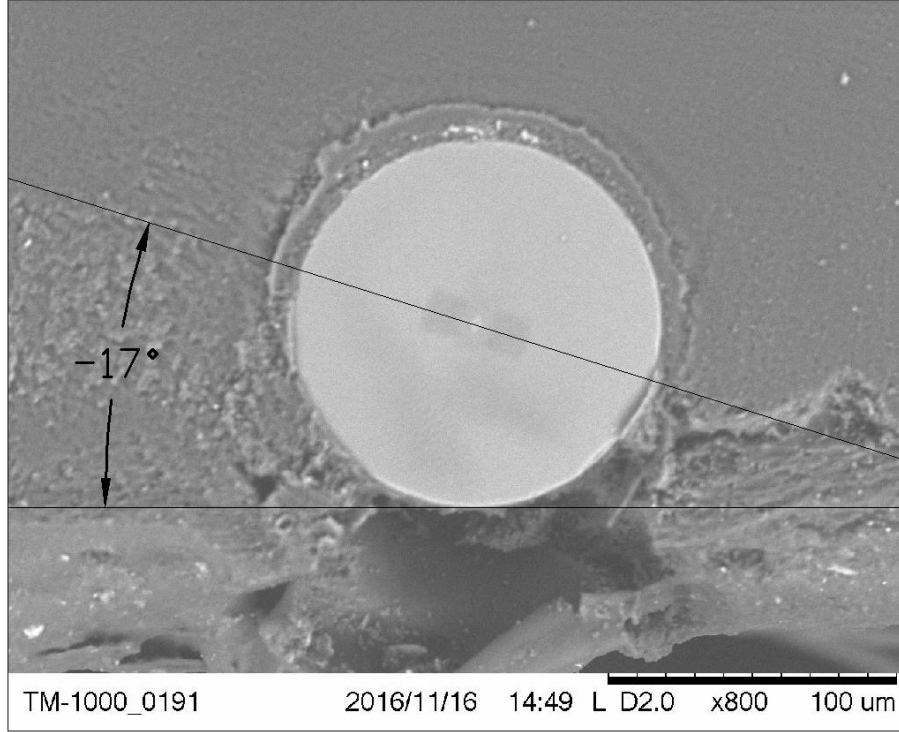


Figure 4.4: Sensor cross-section,  $\varphi = -17^\circ$

Table 4.2: Single PM-FBG Sensor Measurement Percent (%) Error Across Load

Axis	5	20	50	100	150	250	500	1000	1500	2000
$\varepsilon_{xx}$	0	15.03	33.23	14.71	13.78	36.55	61.33	36.15	45.23	25.14
$\varepsilon_{yy}$	0	55.35	0.14	8.66	37.02	18.24	1.92	11.59	15.88	19.14

in bandwidth of  $\lambda_{B_s}$  and  $\lambda_{B_f}$  as the specimen reaches an applied force above 250N. The split is seen in figure 4.3 at the 500N measurement, its corresponding effects on strain are seen in 4.5(a) and 4.5(d). The distortion might be caused by a non-uniform strain across the length of the FBG causing a chirping effect on the FBG as it affects both polarization directions equally. Studies on chirped gratings are beyond the scope of this study, all Bragg shifts  $\Delta\lambda_{B_{s,f}}$  to strain calculations were derived on the basis of the Bragg peak and so this dissertation does the same.

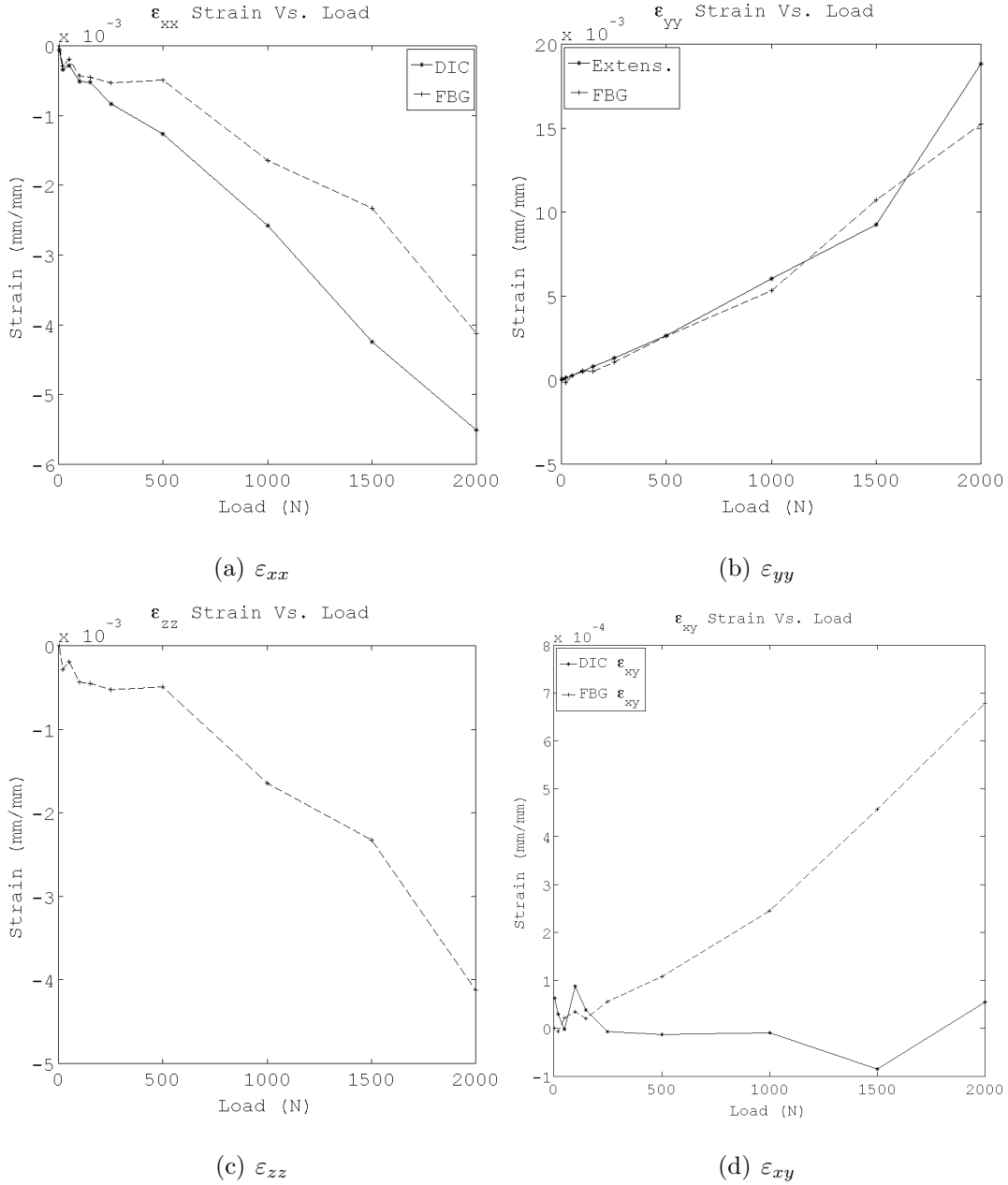
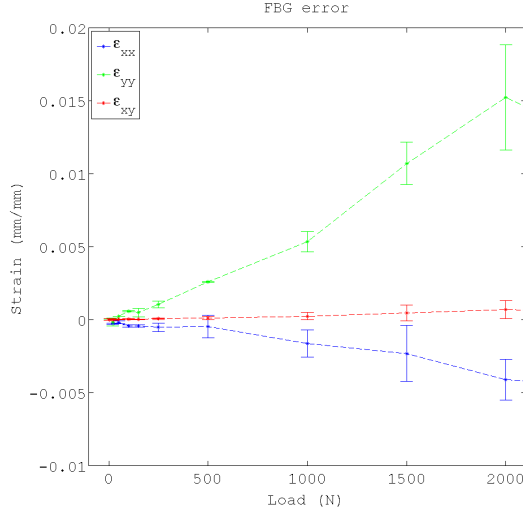


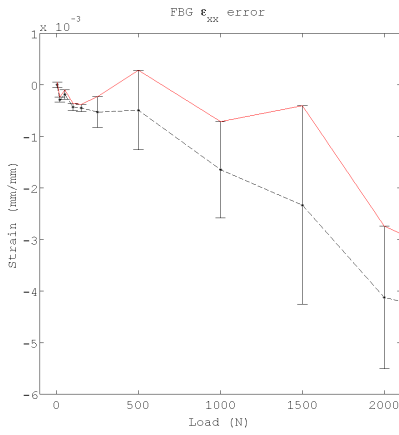
Figure 4.5: Sensor(dashed line) and DIC strain(solid line) or Extensometer in y direction vs. load

## 4.2 PM-FBG Rosette

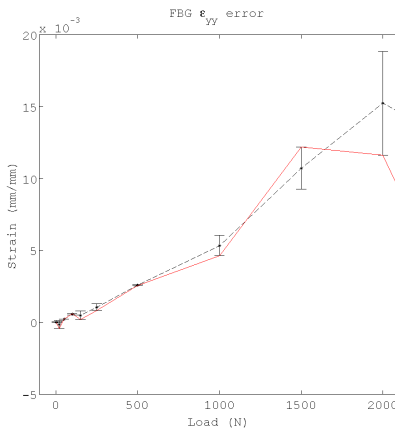
Table 4.3 delineates the location of each sensor on the DIC pixel grid and the angles of  $\epsilon_a$ ,  $\epsilon_s$ , and  $\epsilon_f$  with respect to the primary strain axes  $\epsilon_{xx}$ ,  $\epsilon_{yy}$ , and  $\epsilon_{zz}$  needed to calculate



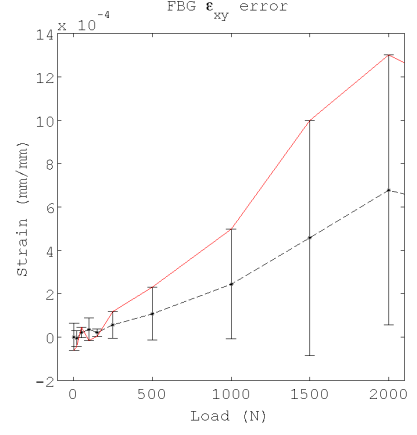
(a) planar Error



(b)  $\epsilon_{xx}$



(c)  $\epsilon_{yy}$



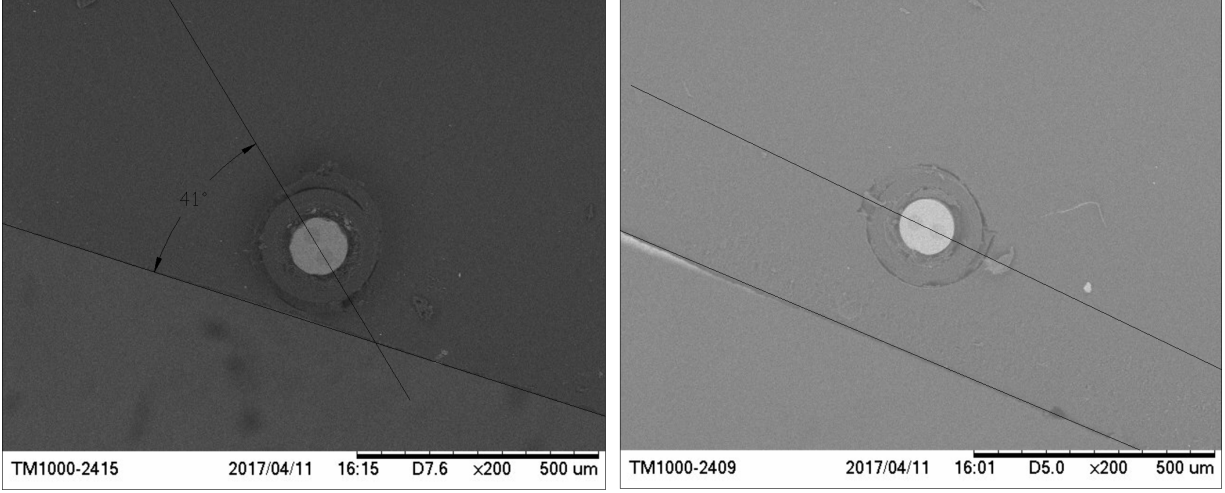
(d)  $\epsilon_{xy}$

Figure 4.6: Single PM-FBG Error across load DIC/Extensometer (dashed) to FBG(red)

the strain transformations for FBG2 and FBG3. The angle  $\phi$  in the table refers to the angle of the PM slow axis with respect to the surface of the specimen and is negative in the counter clockwise direction. The angle  $\theta$  refers to the position of the longitudinal axis of the PM-FBG,  $\epsilon_a$ , with respect to the y axis of the specimen, clockwise being positive. The optical response of FBG2 and FBG3 to the far field strain is shown in figure 4.8. It is apparent in this image the PM-FBG rosette did not undergo the same peak broadening distortion seen in the single PM-FBG experiment. The strain transformation and strain lag

Table 4.3: FBG Rosette Sensor Locations

Sensor	Cross-sectional angle ( $\phi$ )	Axial angle ( $\theta$ )	Pixel Location (x,y)
FBG2 - 1550nm	$-41^\circ$	$90^\circ$	870,758
FBG3 - 1560nm	$0^\circ$	$45^\circ$	870,748



(a) FBG2

(b) FBG3

Figure 4.7: Cross section of FBG 2 and 3 showing distance of sensor to specimen surface.

transfer algorithm described at the begining of chapter 3 was performed on both sensors to calculate the three primary strains  $\varepsilon_{xx}$ ,  $\varepsilon_{yy}$ ,  $\varepsilon_{zz}$  and 2 shear strains  $\varepsilon_{xy}$  and  $\varepsilon_{yz}$ . A formulation of the shear strain  $\varepsilon_{xz}$ , best described as the out-of-plane and fiber longitudinal shear, still remains to be found. The following figures, 4.9 - 4.12, compare the measurements of the PM-FBG rosette to that of its validating mechanical counterpart for each strain tensor elements. For this test, only  $\varepsilon_{xx}$ ,  $\varepsilon_{yy}$  and  $\varepsilon_{xy}$  can be directly validated.  $\varepsilon_{zz}$  and  $\varepsilon_{yz}$  are not measured by the DIC or extensometer, however are used to calculate all other elements and are assumed accurate if  $\varepsilon_{xx}$ ,  $\varepsilon_{yy}$  and  $\varepsilon_{xy}$  calculated from the rosette are accurate representations of the DIC and extensometer measurements.

The  $\varepsilon_{xx}$  measurements from the transformed PM-FBG are in line with the DIC. There's compression (i.e. a negative strain) and the correlation is 0.74 and 0.97 for FBG2 and

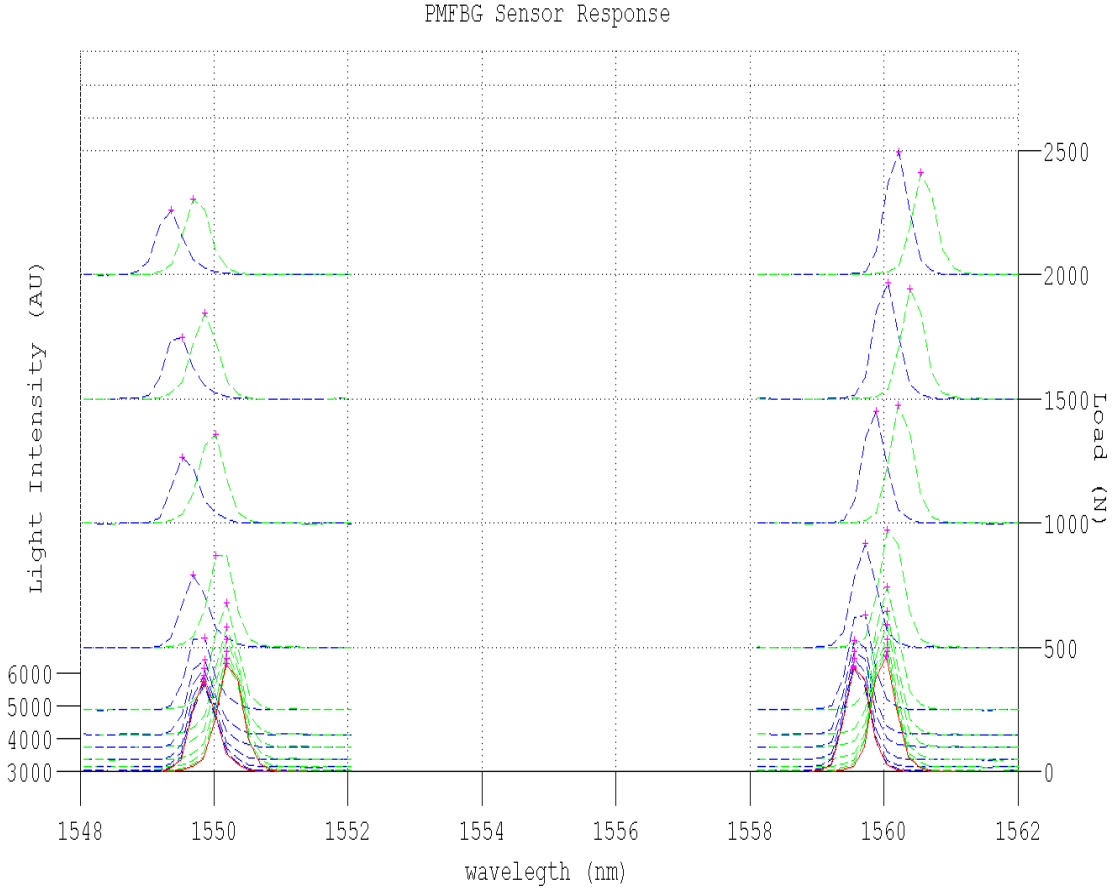


Figure 4.8: Mounted PM-FBG rosette optical wavelength shift response at 0 - 2000 N specimen loads with fast green and slow blue axes. FBG2 is on the right, FBG3 is on the left.

FBG3, respectively.

The  $\varepsilon_{yy}$  PM-FBG measurements are also in agreement with DIC/extensometer measurements. The correlation is 0.99 and 0.96 for FBG2 and FBG3, respectively.

The use of 2 planar, co-located PM-FBG measurements can now be used to accurately reconstruct the planar shear strain  $\varepsilon_{xy}$ . In actually, all that is needed to calculate the planar shear strain is 3 measurements, as implied in equation 3.7. A single PM-FBG cannot do this, however the use of 2 PM-FBGs allows for 4 measurements. In the single PM-FBG experiment, we assumed  $\varepsilon_{x'y'}$  as shown in equation 3.1.2 was zero, this produces

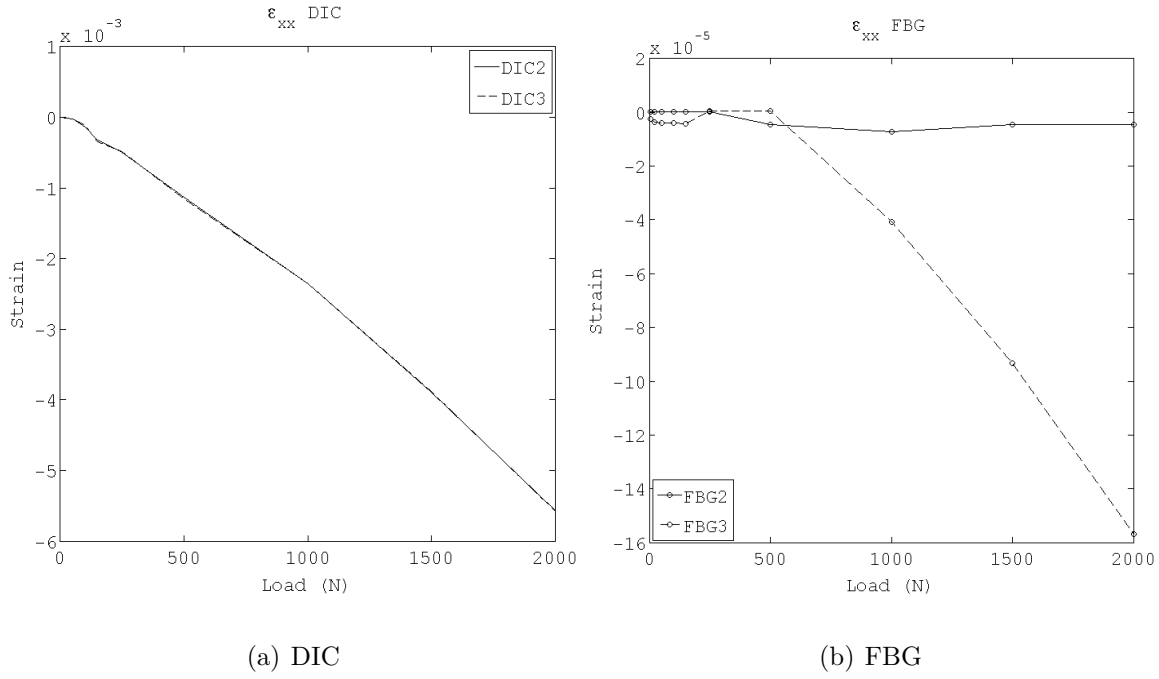


Figure 4.9:  $\epsilon_{xx}$  sensor measurements per strain axis vs. load

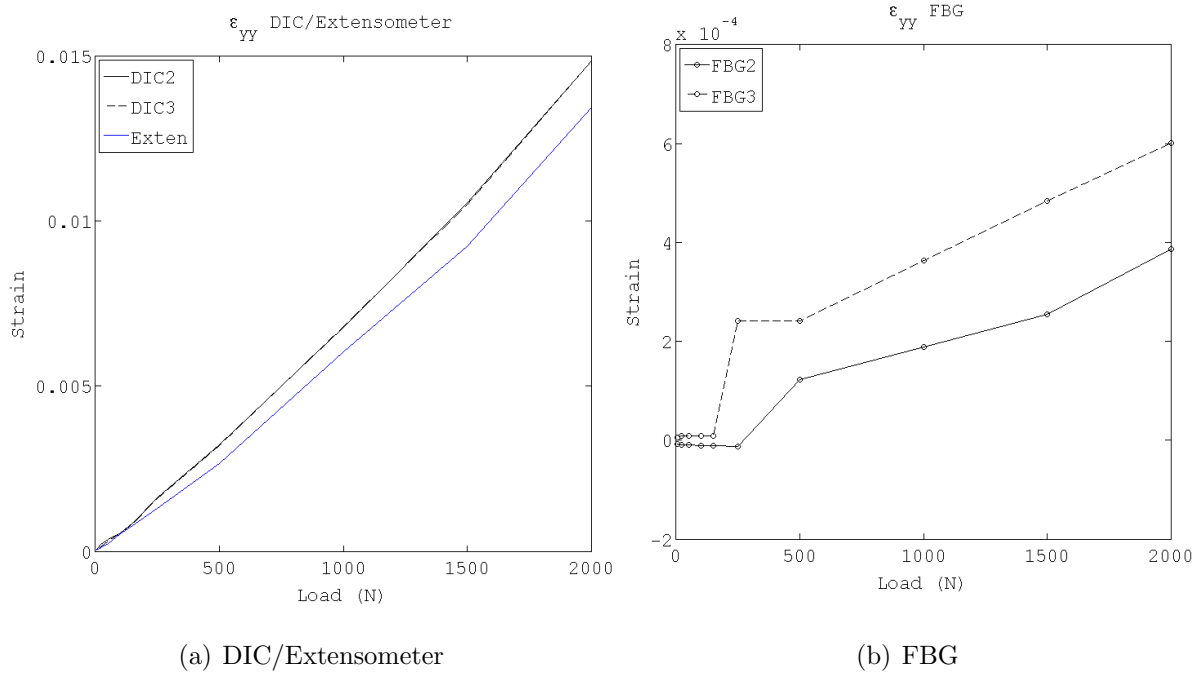


Figure 4.10:  $\epsilon_{yy}$  sensor measurements per strain axis vs. load

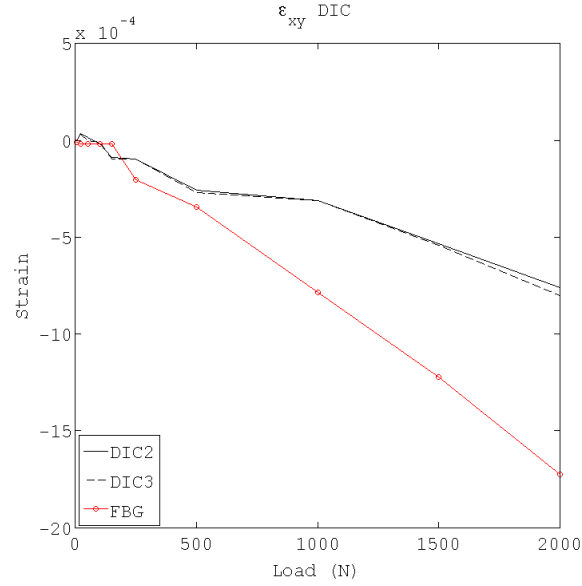


Figure 4.11:  $\varepsilon_{xy}$  sensor measurement per strain axis vs. load

an erroneous  $\varepsilon_{xy}$  measurement. The use of 2 PM-FBGs is needed to accurately measure this strain component. The correlation of this measurement calculation to the DIC analysis is 0.98.

The out-of-plane strain measurements in figure 4.12 show the general trend of the out of plane strain measurements. These cannot be verified at the moment, however measurement trends show compression against the tension in  $\varepsilon_{yy}$ . The table 4.4 lists the average error for all load measurements for both sensors and defines the gauge factor. Gauge factors are on the order or magnitude smaller than the single PM-FBG configuration. This is due to a number of factors including the FBG Acolyte re-coating, and greater distance between the surface and sensors.

The percent error of FBG2 and FBG3 rom the PM-FBG rosette and the DIC/extensometer data of the primary planar strains are listed in table 4.5.



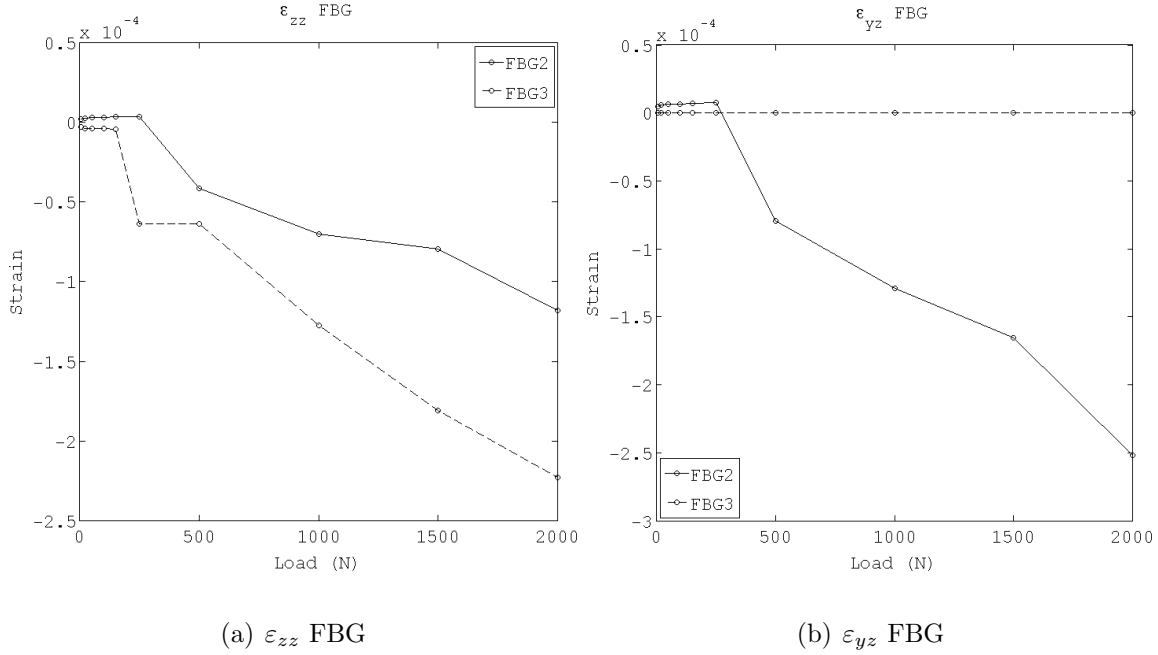


Figure 4.12: Out-of-plane sensor measurements per strain axis vs. load

Table 4.4: Rosette PM-FBG Sensor Measurements Error, Std. Deviation, % Error

Axis	Sensor	Mean Error $\frac{mm}{mm}$	Std. Deviation $\frac{mm}{mm}$	Avg. Gauge Factor
$\epsilon_{xx}$	FBG2	$1.39 \times 10^{-3}$	$1.83 \times 10^{-3}$	-0.1998
	FBG3	$1.39 \times 10^{-3}$	$1.84 \times 10^{-3}$	-0.0654
$\epsilon_{yy}$	FBG2	$3.35 \times 10^{-3}$	$4.27 \times 10^{-3}$	0.0163
	FBG3	$3.24 \times 10^{-3}$	$4.21 \times 10^{-3}$	0.0402
$\epsilon_{xy}$	-	$2.28 \times 10^{-4}$	$3.24 \times 10^{-4}$	-

Table 4.5: Rosette PM-FBG Sensor Measurement Percent (%) Error Across Load

Axis	Sensor	5	20	50	100	150	250	500	1000	1500	2000
$\epsilon_{xx}$	FBG2	20.61	20.17	20.10	20.01	19.99	19.99	19.90	19.92	19.95	19.96
	FBG3	6.30	6.71	6.59	6.55	6.54	6.54	6.51	6.52	6.53	6.53
$\epsilon_{yy}$	FBG2	1.83	1.70	1.67	1.66	1.65	1.64	1.57	1.58	1.59	1.59
	FBG3	3.13	3.78	3.91	3.96	3.98	3.41	3.72	3.81	3.84	3.86

# Chapter 5

## Concluding Remarks

This research sought out to build a full state of strain using Bragg gratings written in polarization maintaining optical fiber. The interrogation technique, strain transformation algorithms and topologies presented in this dissertation and in figure 5.1

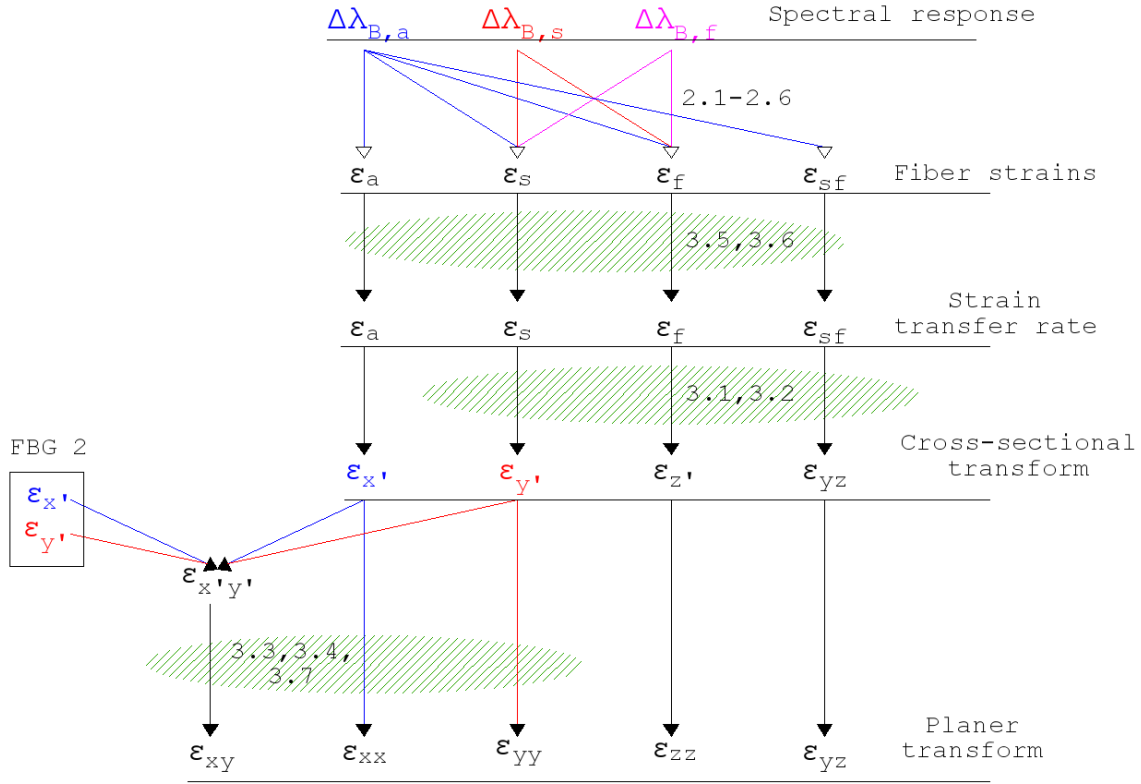


Figure 5.1: Strain evaluation algorithm

are the culmination of research not before attempted. The primary strains  $\epsilon_{xx}$ ,  $\epsilon_{yy}$ ,  $\epsilon_{zz}$  and the shear strains  $\epsilon_{xy}$ ,  $\epsilon_{yz}$  of the polycarbonate specimen under uniaxial tension were reconstructed with a percent error of less than 10% across increasing load. Missing was the

component  $\varepsilon_{xz}$  of the full tensor reconstruction:

$$\varepsilon = \begin{bmatrix} \varepsilon_{xx} & \varepsilon_{xy} & n/a \\ \varepsilon_{yx} & \varepsilon_{yy} & \varepsilon_{yz} \\ n/a & \varepsilon_{zy} & \varepsilon_{zz} \end{bmatrix} \quad (5.1)$$

The optical interrogation system presented here is practical and inexpensive. However, a multiple input spectrometer is required for real-time, continuous strain sensing. The use of two inputs allows for simplified polarization direction discrimination and therefore strain calculation. The strain observed by the single and rosette PM-FBGs showed strong Pearson linear correlations when compared to DIC and extensometer measurements. These were in the order of 0.97 for the planar strain directions  $\varepsilon_{xx}$ ,  $\varepsilon_{yy}$ , and  $\varepsilon_{xy}$ . Percent error for the planar remained under 20% with the caveat that sensor placement and material composition play a role on the sensitivity of the PM-FBG. This is evident as we compare the gauge factor for both experiments and notice an order of magnitude difference between them. The error introduced in the single PM-FBG experiment is due to strain gradients present on the FBG region causing the Bragg peak to widen. This increased the mean error upwards of 66% in some measurements. This discrepancy might be due to experimental differences such as FBG re-coating and/or placement with respect to the distance from the specimen surface.

The use of this type of fiber sensor still faces challenges, most notably, the requirement to know the orientation of the polarization axes with respect to a surface of the structure. Without this information, the advantages of the PM FBG sensor are completely lost. Other challenges include the inability of the sensor to measure any shear strain with respect to its longitudinal axis, which translates to the inability of a single sensor to directly measure shear strain in the plane to which it is installed. Therefore, more than one PM FBG is required to measure a full state of strain on a structure. An advantage of PM FBGs still remains over conventional uniaxial optical fiber sensors as interrogation complexity and cost deferrer minimally. Acknowledging these challenges, the PM FBG strain sensor still

holds promising sensing capabilities as, 3-dimensional strain sensor.

## 5.1 Future Work

The challenges of this research vary in complexity and scope. A simple improvement on the optical interrogation system would be the use of a spectral analyzer with two independent inputs. This would reduce the need for optical switches and redundant polarization devices. Pérez Grassi mentions the trend of research in optical sensing as the need to construct a full state of strain at the point of sensing. This research leaves building a three-dimensional strain tensor with PM FBG sensors for future work. A full strain tensor cannot be built by a single PMFBG or by not knowing the cross sectional rotational orientation of a polarization axis with respect to the surface. This is, arguably the biggest challenge facing the wide spread implementation of the PMFBG, what use is a sensor if one has to destroy it to properly analyze it? Using of Carrier Phase Synchronization, a digital communications technique [42], to estimate the rotation of the polarization axis analogous to, for example a square 8-PSK constellation is a possible solution. This can be done by considering the polarization coupling in the optical signals of cross-section shear measurements  $\varepsilon_{xy,yx}$  as inputs for the phase locked loop.

# References

- [1] Mazumdar, S. (2001). *Composites manufacturing: materials, product, and process engineering*. CrC press.
- [2] Mawatari, T., & Nelson, D. (2008). A multi-parameter Bragg grating fiber optic sensor and triaxial strain measurement. *Smart Materials and Structures*, 17(3), 035033.
- [3] Udd, E., Nelson, D. V., Lawrence, C. M., & Ferguson, B. A. (1996, May). Three-axis strain and temperature fiber optic grating sensor. In *1996 Symposium on Smart Structures and Materials* (pp. 104-109). International Society for Optics and Photonics.
- [4] Kirkby, E., De Oliveira, R., Michaud, V., & Månson, J. A. (2011). Impact localisation with FBG for a self-healing carbon fibre composite structure. *Composite Structures*, 94(1), 8-14.
- [5] Yariv, A., & Yeh, P. (2007). *Photonics: optical electronics in modern communications* (Vol. 6). New York: oxford university press.
- [6] Born, M., & Wolf, E. (1980). *Principles of optics: electromagnetic theory of propagation, interference and diffraction of light*. Elsevier.
- [7] Kliger, D. S., Lewis, J. W., Randall, C. E., & Azzam, R. M. (1991). *Polarized Light in Optics and Spectroscopy*.
- [8] R. Rumpf, *Lecture 2 (CEM) - Maxwell's Equations*, 2013. [Online]. Available: <https://www.youtube.com/watch?v=JOgtCeUMIAc>. [Accessed: 4- Apr- 2017]
- [9] Saleh, B. E., Teich, M. C., & Saleh, B. E. (1991). *Fundamentals of photonics* (Vol. 22). New York: Wiley.

- [10] Ramaswami, R., Sivarajan, K., & Sasaki, G. (2009). *Optical networks: a practical perspective*. Morgan Kaufmann.
- [11] Hecht, J. (2015). *Understanding fiber optics*. Jeff Hecht.
- [12] R. Rumpf, *Lecture 3 (CEM) - Electromagnetic Principles*, 2013. [Online]. Available: <https://www.youtube.com/watch?v=2mlfwMzuT0g>. [Accessed: 5- Apr- 2017]
- [13] Bertram, A., & Glüge, R. (2015). ONE-DIMENSIONAL MATERIAL THEORY. In *Solid Mechanics* (pp. 1-42). Springer International Publishing.
- [14] Bedford, A., Fowler, W. L., & Liechti, K. M. (2003). *Statics and mechanics of materials*. Prentice Hall/Pearson Education.
- [15] Cozzarelli, F. A., & Shames, I. H. (1992). Elastic and Inelastic Stress Analysis.
- [16] Murray, W. M., & Miller, W. R. (1992). *The bonded electrical resistance strain gage: an introduction*. Oxford University Press.
- [17] Timoshenko, S., & Woinowsky-Krieger, S. (1959). Theory of plates and shells.
- [18] Kersey, A. D. (1996). A review of recent developments in fiber optic sensor technology. *Optical fiber technology*, 2(3), 291-317.
- [19] Bertholds, A., & Dandliker, R. (1988). Determination of the individual strain-optic coefficients in single-mode optical fibres. *Journal of lightwave technology*, 6(1), 17-20.
- [20] Quintana, J., & Gonzalez, V. (2014, April). Detection and calculation of reflected spectral shifts in fiber-Bragg gratings (FBG) in polarization maintaining optical fiber. In *SPIE Smart Structures and Materials+ Nondestructive Evaluation and Health Monitoring* (pp. 90614D-90614D). International Society for Optics and Photonics.
- [21] Müller, M. S., Buck, T. C., El-Khozondar, H. J., & Koch, A. W. (2009). Shear strain influence on fiber Bragg grating measurement systems. *Journal of Lightwave Technology*, 27(23), 5223-5229.

- [22] Bernardini, A., El-Khozondar, H. J., & Koch, A. W. (2011). Method for strain tensor reconstruction with embedded fiber Bragg grating sensors. *Smart Materials and structures*, 20(10), 105031.
- [23] Okamoto, K., Hosaka, T., & Eda Hiro, T. (1981). Stress analysis of optical fibers by a finite element method. *IEEE Journal of Quantum Electronics*, 17(10), 2123-2129.
- [24] Bertholds, A., & Dandliker, R. (1988). Determination of the individual strain-optic coefficients in single-mode optical fibres. *Journal of lightwave technology*, 6(1), 17-20.
- [25] Hill, K. O., & Meltz, G. (1997). Fiber Bragg grating technology fundamentals and overview. *Journal of lightwave technology*, 15(8), 1263-1276.
- [26] Maier, R. R., MacPherson, W. N., Barton, J. S., Jones, J. D., McCulloch, S., & Burnell, G. (2004). Temperature dependence of the stress response of fibre Bragg gratings. *Measurement Science and Technology*, 15(8), 1601.
- [27] Lawrence, C. M. (1997). Embedded fiber-optic strain sensors for process monitoring of composites.
- [28] Prabhugoud, M., & Peters, K. (2006). Finite element model for embedded fiber Bragg grating sensor. *Smart materials and structures*, 15(2), 550.
- [29] Mawatari, T., & Nelson, D. (2008). A multi-parameter Bragg grating fiber optic sensor and triaxial strain measurement. *Smart Materials and Structures*, 17(3), 035033.
- [30] Bosia, F., Giaccari, P., Botsis, J., Facchini, M., Limberger, H. G., & Salathé, R. P. (2003). Characterization of the response of fibre Bragg grating sensors subjected to a two-dimensional strain field. *Smart materials and Structures*, 12(6), 925.
- [31] Müller, M. S., Buck, T. C., El-Khozondar, H. J., & Koch, A. W. (2009). Shear strain influence on fiber Bragg grating measurement systems. *Journal of Lightwave Technology*, 27(23), 5223-5229.

- [32] Chu, P., & Sammut, R. (1984). Analytical method for calculation of stresses and material birefringence in polarization-maintaining optical fiber. *Journal of lightwave technology*, 2(5), 650-662.
- [33] Wagreich, R. B., Atia, W. A., Singh, H., & Sirkis, J. S. (1996). Effects of diametric load on fibre Bragg gratings fabricated in low birefringent fibre. *Electronics letters*, 32(13), 1223-1224.
- [34] Ansari, F., & Libo, Y. (1998). Mechanics of bond and interface shear transfer in optical fiber sensors. *Journal of engineering mechanics*, 124(4), 385-394.
- [35] Udd, E., Schulz, W. L., Seim, J. M., Haugse, E. D., Trego, A., Johnson, P. E., & Makino, A. (2000, June). Multidimensional strain field measurements using fiber optic grating sensors. In *SPIE's 7th Annual International Symposium on Smart Structures and Materials* (pp. 254-262). International Society for Optics and Photonics.
- [36] Li, D., Li, H., Ren, L., & Song, G. (2006). Strain transferring analysis of fiber Bragg grating sensors. *Optical engineering*, 45(2), 024402-024402.
- [37] Li, H. N., Zhou, G. D., Ren, L., & Li, D. S. (2007). Strain transfer analysis of embedded fiber Bragg grating sensor under nonaxial stress. *Optical Engineering*, 46(5), 054402-054402.
- [38] Müller, M. S., Hoffmann, L., Sandmair, A., & Koch, A. W. (2009). Full strain tensor treatment of fiber Bragg grating sensors. *IEEE Journal of Quantum Electronics*, 45(5), 547-553.
- [39] Botero-Cadavid, J. F., Causado-Buelvas, J. D., & Torres, P. (2010). Spectral properties of locally pressed fiber Bragg gratings written in polarization maintaining fibers. *Journal of lightwave technology*, 28(9), 1291-1297.
- [40] Quintana, J., Rumpf, R., & Gonzalez, V. (2014, March). Modified transfer matrix method model for a fiber Bragg grating strain sensor in polarization maintaining single



mode optical fiber. In *SPIE OPTO* (pp. 89881B-89881B). International Society for Optics and Photonics.

- [41] Müller, M. S., El-Khozondar, H. J., Buck, T. C., & Koch, A. W. (2009). Analytical solution of four-mode coupling in shear strain loaded fiber Bragg grating sensors. *Optics letters*, 34(17), 2622-2624.
- [42] Rice, M. (2009). *Digital communications: a discrete-time approach*. Pearson Education India.

# Appendix A

## Glossary

ASTM - American Society for Testing and Materials

DIC - Digital Image Correlation

$\varepsilon_{xx,yy,zz,xy,xz,yz}$  - Specimen Strains

$\varepsilon_{a,f,s,sf}$  - Optical Fiber Strains

EMI - Electromagnetic Interference

FBG - Fiber Bragg Gratings

FC/APC - Fiber Optic Connector Angled Physical Contact

FOS - Fiber Optic Sensors

N - Newton(unit)

PANDA - Polarization Maintaining Optical Fiber type

PM - Polarization Maintaining

PM-FBG - Polarization Maintaining Fiber Bragg Grating

SHM - Structural Health Monitoring

SLD - Superluminescent Diode

SM - Single Mode

# Curriculum Vitae

Joel Quintana earned his Bachelors and Masters of Science in Electrical Engineering from the University of Texas at El Paso in 2006 and 2009 respectively. In 2012 he joined the doctoral program in Electrical and Computer Engineering at UTEP as well. Prior to joining the doctoral program, Dr. Quintana worked professionally for Raytheon and Lockheed Martin Companies in White Sands Missile Range and toured the United States and Canada playing for the band The Royalty. During his candidacy, Dr. Quintana studied the application of optical fiber and sensor technologies. His dissertation on the characterization of fiber Bragg grating (FBG) sensors was funded in part by NASA Marshall Space Center. He has presented at SPIE Smart Structures and Photonics West Conferences. Dr. Quintana received various awards, including the Mike Loya Commercialization Fellows Endowment, University of Texas at El Paso Graduate Scholarship Fund and the Texas Instruments Foundation Endowed Scholarship. Dr. Quintana is co-inventor of the Arsenic Canary - An Arsenic Concentration Detection System and co-founder of Minus Tau, an optical sensing technology for measurement of concussive impact during contact sports.

Permanent address: 1124 N. El Paso St. Apartment 4

El Paso, Texas 79902-4927